PHYSIK-DEPARTMENT

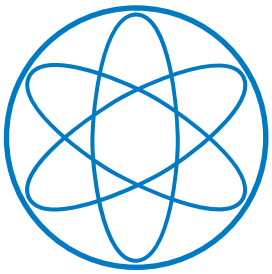

Study of an antideuteron production mechanism and propagation through the interstellar medium

Master's Thesis
by
Maximilian Horst

Dense and Strange Hadronic Matter group E62
Prof. Laura Fabbietti
01.10.2021

TECHNISCHE UNIVERSITÄT MÜNCHEN

Abstract

Coalescence is one of the main models used to describe the formation of light (anti)nuclei in high-energy collisions. It is based on the assumption that two nucleons close in phase-space can coalesce and form a nucleus. Coalescence has been successfully tested in hadron collisions with various experiments, from small (proton proton collisions) to large collision systems (Au–Au and Pb–Pb collisions). However, in Monte Carlo (MC) simulations (anti)nuclear production is typically not described by event generators. A possible solution is given by the implementation of so-called coalescence afterburners, which can describe nuclear production on an event-by-event basis. This idea finds its application especially in astrophysical studies, allowing for precise description of expected (anti)nuclear fluxes in cosmic rays, which are crucial for indirect Dark Matter searches.
In this thesis the implementation of event-by-event coalescence afterburners for MC generators is presented. Different approaches to this implementation will be discussed, namely the spherical approximation and the coalescence approach using the deuteron Wigner function. A comparison with available experimental results from various collision systems is presented. Additionally, the antiproton production in the event generator EPOS 3 is compared to measurements and a correction scheme is developed. This correction scheme allows to test the actual quality of the coalescence approach, free from biases of the event generator.

Contents

1 Introduction **1**

2 Light nuclei production **7**
2.1 Space-time evolution of a nuclear collision . . . 7
2.2 Production models . . . 8
2.2.1 Thermal model . . . 8
2.2.2 Coalescence model . . . 9
Classical coalescence . . . 9
Coalescence using the Wigner function . . . 11
2.2.3 Problems of the coalescence model . . . 13
The value of the coalescence momentum . . . 13
Momentum conservation . . . 14
2.2.4 Comparison of coalescence and thermal model . . . 15
2.3 Existing antideuteron cosmic ray predictions . . . 15

3 The EPOS event generator **17**
3.1 Working principle of EPOS . . . 17
3.2 EPOS event output . . . 18

4 Tuning EPOS to antiproton data **23**
4.1 pp collisions . . . 24
4.1.1 NA61/SHINE . . . 24
4.1.2 NA49 . . . 26
4.1.3 BRAHMS . . . 29
4.1.4 STAR . . . 29
4.2 Other colliding systems . . . 30
4.2.1 NA49 p–C . . . 31
4.2.2 LHCb p–He . . . 32
4.2.3 STAR Au–Au . . . 33
4.3 Antiprotons from hyperon decays . . . 35
4.4 Summary of antiproton data . . . 36
4.5 Correction scheme . . . 36
4.6 Corrected results . . . 40
4.7 Summary of spline interpolation . . . 41

5 Anti-Deuteron production in EPOS **43**
5.1 Available experimental data 43
5.2 STAR Au–Au 44
5.3 ALICE pp 13 TeV high multiplicity 47

6 Summary and Outlook **51**

A Appendix A - Measurement results and EPOS predictions **53**
A.1 NA61 53
A.2 NA49 54
A.3 LHCb p–He 54

B Appendix B - EPOS **57**
B.1 Impact parameter in EPOS 57
B.2 Concrete examples for particle groups of interest 57

Bibliography **59**

Chapter 1

Introduction

Dark Matter was first proposed by Fritz Zwicky [1] as an explanation to the high velocity dispersion observed inside the Coma cluster, a nearby galaxy cluster[1], of ~ 1000 km/s. From the virial theorem, applied on the mass of only visible objects he obtained a velocity dispersion of only 80km/s. From this it was concluded that a large percentage of the mass must be from non-luminous matter, which he called dark matter. In a second assessment of the problem a velocity dispersion[2] of 700km/s, the number of observed galaxies, 1000, as well as the size of the cluster, which was estimated to be about $\sim 10^6$ ly, was used. As a result, an average mass per galaxy of $4 \times 10^{10} M_{\odot}$ was obtained which is almost three orders of magnitude larger than the absolute average luminosity per galaxy which was assessed to be about 8.5×10^7 times the solar luminosity. Future reassessments relaxed this discrepancy by about a factor of 8 [2]. Further explanations of this phenomenon, like the hypothesis that galaxy clusters are unstable expanding objects or ionized gas in the gravitational focus of the cluster were disproven [2]. When Rogstad and Shostak [3] published the first rotation curves of galaxies in 1972 , it was evident that there must be a non-luminous matter inside these galaxies, that extends towards the edges of these galaxies and beyond. These findings were later confirmed by Bosma [4] and Rubin et al. [5]. These observations were the first strong evidence for the existence of dark matter. At the time, however, dark matter was referring to all astrophysical non-luminous objects like white dwarves and neutron stars. Nowadays dark matter strictly refers to non-baryonic, elementary particles [6]. The most promising candidates for dark matter include Weakly Interacting Massive Particles (WIMPs), Superpartners and Axions [7].
Fig. 1.1 shows possible dark matter candidates in the mass vs interaction cross section plane. As a reference, the standard model neutrino with a mass of ≈ 0.1 eV and and interaction cross section of 1 pb is shown. The red, pink and blue colors represent hot dark matter (HDM), warm dark matter (WDM) and cold dark matter (CDM), respectively. In a theory of HDM the dark matter particles travel at ultrarelativistic velocities, while in a theory of CDM the dark matter particles travel much slower compared to the speed of light. A theory of WDM predicts velocities between these two extremes. It is evident that dark matter searches need to cover a large possible phase-space with 30 orders of magnitude for their mass and 40 orders of interaction cross section.
So far no dark matter particle was measured. In general, approaches to detect dark matter

[1] Further information on the Coma Cluster: https://sci.esa.int/web/planck/-/47695-the-coma-cluster
[2] Outliers were filtered out which were believed to not be part of the bound cluster, but passing objects

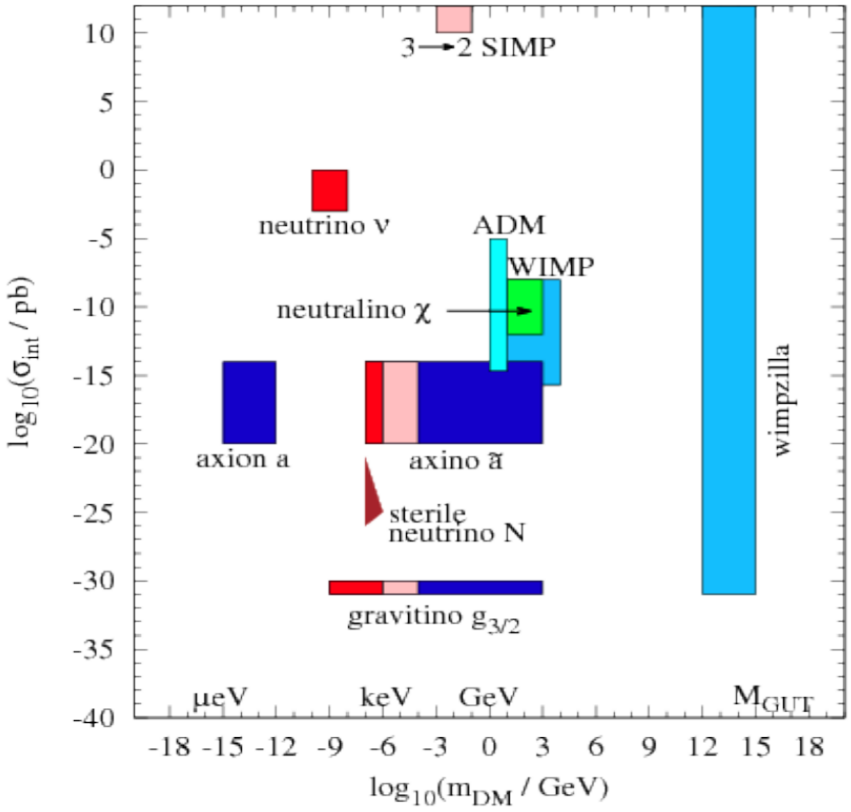

Figure 1.1 Several candidates of dark matter are shown in the plane of dark matter mass and σ_{int} representing the typical strength of interactions with ordinary matter. The red, pink and blue colors represent predictions for hot dark matter (HDM), warm dark matter (WDM) and cold dark matter (CDM) respectively. Taken from [8].

candidates can be separated into experiments in particle colliders as well as direct and indirect methods [7, 6]. In the first method, dark matter particles would be created in collider experiments. The dark matter particle would either escape the collider without interacting with it and carry away energy, or the particle could decay into standard model particles inside the detector, leaving a signal in the invariant mass spectra of the decay products. In direct dark matter detection methods, as the name suggests, the dark matter particle is measured directly. This means experiments either measure the recoil of a standard model particle from a collision with a dark matter particle in the case of WIMPs and superpartners, or they measure photons in the case of axions[3]. Recoil experiments usually try to interact with galactic dark matter, while in the case of axions they are created in a lab.
Indirect dark matter detection methods mean that one measures the decay products of dark matter particles in space. The most common idea is that two dark matter particles (Majorana) or one dark matter particle and one antiparticle (Dirac) will annihilate and create standard model particles. These particles will then become part of cosmic rays which can be detected at Earth. Most common probes for cosmic rays from dark matter are photons, positrons or antinuclei. Here antinuclei are the more promising probe compared to their matter counter-

[3]The Peccei-Quinn axion can be transformed into two photons under strong magnetic fields.

parts, since normal nuclei can be created in spallation processes which will dominate other production channels. In addition to the *primary* production from dark matter annihilation, the most common other production channel is *secondary* production in collisions between cosmic rays and the interstellar medium, both of which consist mainly of protons and ^{4}He. Additionally, a *tertiary* contribution from rescattered antinuclei can be expected.
A sketch of production mechanisms of antinuclei in the galaxy can be seen in Fig. 1.2. It shows

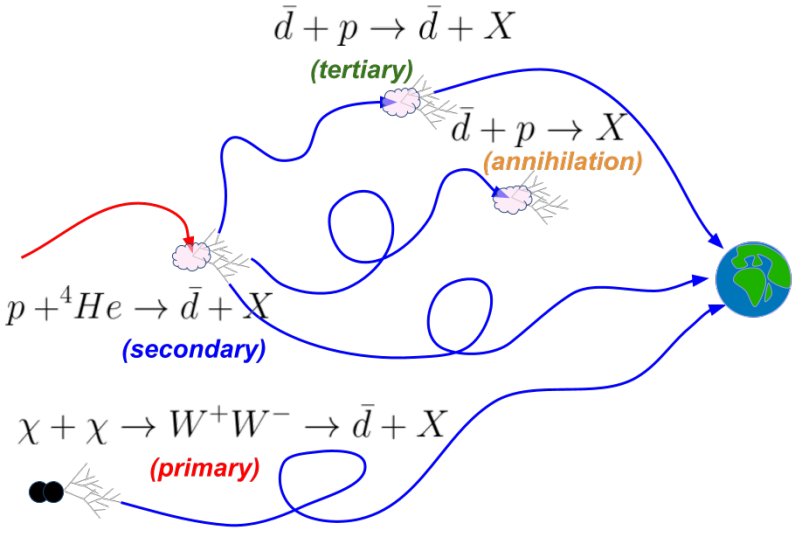

Figure 1.2 Schematic overview of antideuteron production in the galaxy. Primary antideuterons can be produced e.g. by two dark matter particles annihilating into a W^+W^- pair which further decays into an antideuteron and other byproducts. Secondary production occurs when cosmic rays collide with particles from the interstellar medium inelastically and create among other particles an antideuteron. Tertiary antideuterons are secondary antideuterons which scatter off the interstellar medium elastically and a loose significant amount of momentum. This shifts their momenta to lower values than secondaries. Furthermore annihilation of antideuterons with matter from the interstellar medium can occur. Primary, secondary and tertiary antideuterons can be measured at Earth as cosmic rays.

primary antideuterons coming from dark matter annihilation into a W^+W^- pair which further decays into hadrons [9]. Furthermore it shows the secondary production from a cosmic-ray particle, e.g. a proton which collides with a ^{4}He nucleus in the interstellar medium. Tertiary contributions come from secondary antinuclei scattering with particles in the interstellar medium and transferring momentum. Their momentum distribution is shifted towards lower momenta compared to antinuclei from secondary production. In addition to antinuclear production, annihilation can occur when an antinucleus collides with a matter nucleus in the interstellar medium.
All of these three contribution channels make up the antideuteron flux that can be measured at Earth. The separated expected contributions to the overall flux at Earth from primary and secondary antideuterons can be seen in Fig. 1.3. It shows the predictions for generic dark matter annihilation into $b\bar{b}$[9]. For all dark matter candidates, the signal to background ratio is expected to be at least three to four orders of magnitude at low kinetic energy, making antideuterons a great probe for indirect dark matter search. The figure also shows the large uncertainties of these predictions. These uncertainties can be separated into two types. One type are the astrophysical uncertainties, which mainly consider the propagation of cosmic rays through the interstellar medium. The second type comes from the nuclear physics and

mainly deals with the annihilation cross section of antideuterons and the nuclear production yields. However, the uncertainties shown are only from the propagation model, whereas uncertainties from the nuclear production can be estimated by comparing the two panels. In this study the coalescence model explained in Chapter 2.2.2 was used. The left panel shows the prediction for a coalescence momentum of 160 MeV/c while the right panel shows the prediction for 248 MeV/c. Such an increase in coalescence momentum makes the expected flux larger by around a factor of 4, since the overall flux depends on the third power of the coalescence momentum.
Fig. 1.4 shows the predicted antideuteron flux divided by the expected GAPS sensitivity of $2\times10^{-6}\mathrm{m}^2\mathrm{s}^{-1}\mathrm{sr}^{-1}(\mathrm{GeV/n})^{-1}$ for different assumptions made in the nuclear production model. Fig. 1.4a shows that the flux changes by factor of 4 depending on the coalescence momentum

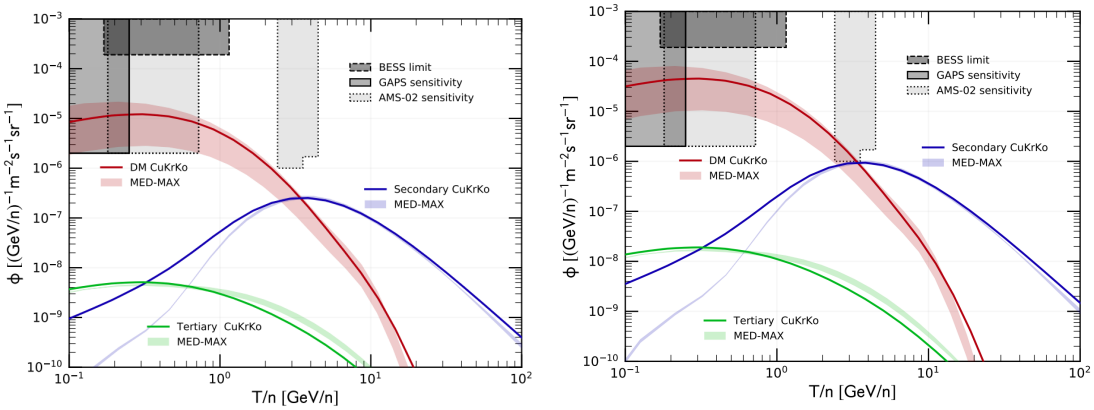

Figure 1.3 Antideuteron flux for secondaries and tertiaries in the ISM and the potential dark matter signal, corresponding to generic $b\bar{b}$ annihilation. The DM signal is restrained using the prediction by Cuoco, Krämer and Korsmeier (CuKrKo) [10]. The propagation models used correspond to the MED and MAX models from [11]. Solar modulation is treated in the force-field approximation, with a potential $\phi = 400$ MV. The predictions are compared to the limits by BESS [12], AMS-02 [13] and GAPS [14]. Both predictions are obtained using an analytical spherical approximation model with $p_0 = 160$ MeV/c (left panel) and $p_0 = 248$ MeV/c (right panel). Taken from [15].

used. Fig. 1.4b shows that the variation between using an analytical approach or a Monte Carlo approach to coalescence changes the expected flux again by a factor of 4.
Furthermore in this study the event generator Pythia was used, which introduces another systematic bias, since event generators are known to not perfectly describe nature.
In order to interpret measurement results of antideuterons in cosmic rays, one needs to understand the secondary and tertiary contributions as precise as possible. As discussed above, the predictions of this background have large uncertainties attributed to them, which are driven by the nuclear formation mechanism and is the main topic of this thesis.
In this thesis, first the concept of light nuclei formation is introduced in Chapter 2. In Chapter 3 the EPOS 3 event generator, which is used throughout the thesis, is discussed. Chapter 4 covers antinucleon production in the EPOS 3 event generator and comparisons with experimental data. Sec. 4.4 introduces a scheme to correct the antinucleon production. Finally, Chapter 5 presents the results of antideuteron production in EPOS 3 using an afterburner developed as part of this thesis.

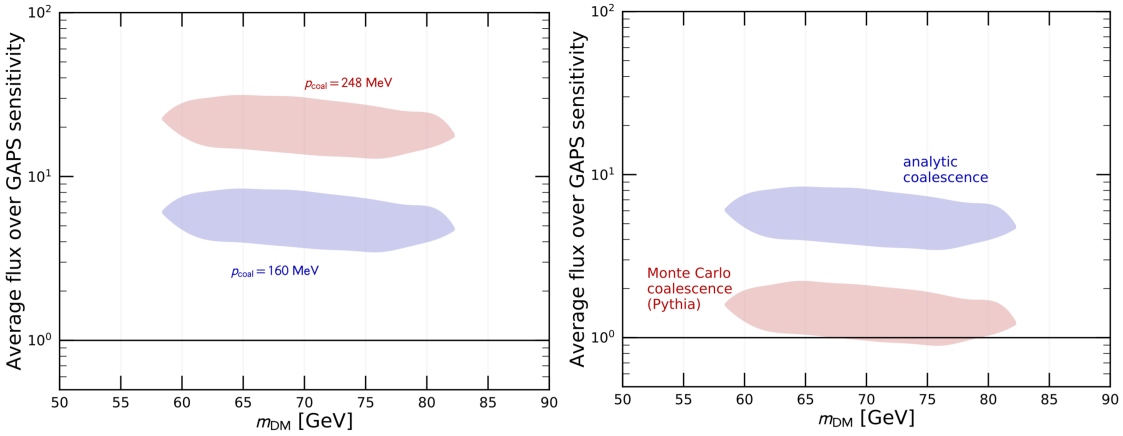

Figure 1.4 Comparison of predictions for antideuteron fluxes divided by the GAPS sensitivity of $2.0 \times 10^{-6}\mathrm{m}^{-2}\mathrm{s}^{-1}\mathrm{sr}^{-1}(\mathrm{GeV/n})^{-1}$ for different coalescence models. The areas correspond to 2σ uncertainty. In panel (a) coalescence momenta of 160 MeV/c and 248 MeV/c are compared. In panel (b) an analytic coalescence model is compared with a Monte Carlo based coalescence. Both use a coalescence momentum of 160 MeV/c. Taken from [15].

Chapter 2

Light nuclei production

In order to investigate the production of light (anti)[1] nuclei in an event generator, the mechanism of nuclear production must be discussed first. Two classes of phenomenological models are available, namely the thermal model and the coalescence model. A short description of both are given in this chapter.

2.1 Space-time evolution of a nuclear collision

Before discussing the production models of light nuclei, one first has to establish the current understanding of the space-time evolution of a high-energy hadron collision. The two possible scenarios are shown in Fig. 2.1 [16, 17].
After a heavy-ion or high energy collision, the system is in a pre-equilibrium stage. This stage is dominated by hard processes, which are characterized by a high momentum transfer between scattering partons creating either particles with large transverse momenta or large masses. These particles rescatter elastically and inelastically. This leads the system to reach thermal equilibrium and if the energy of the collision is high enough, a Quark-Gluon-Plasma (QGP) is formed. Otherwise the free partons will directly form a Hadron Resonance Gas (HRG). The QGP has thermal pressure gradients coming from anisotropies in the initial collision. These lead to a collective expansion of the system and is described by relativistic hydrodynamics. With this expansion the energy density and its temperature decreases. Once the energy density reaches a critical value of $\epsilon_c \simeq 1\text{GeV/fm}^3$ the QGP undergoes a phase transition into a HRG which further expands and cools down. At the point it reaches the chemical freeze-out, characterized by the critical temperature t_{chem}, the energy of the individual particles in the hadron gas is no longer high enough to scatter inelastically. At this point the abundances of particles species are fixed, barring decays of unstable particles and resonances. After the chemical freeze-out the volume of the hadron gas further increases, reducing its density, while the particles further scatter elastically. Once the mean free path of particles exceeds the size of the system, even elastic scattering no longer occurs. At this so-called kinetic freeze-out, the kinematic distribution of particles in the final state is fixed.
In small colliding systems and lower energy collisions the energy is not high enough to form a QGP, instead the system directly forms a HRG and from then on evolve in the exact same way.

[1] Since the mechanisms to form nuclei and antinuclei are equivalent, from now on the prefix anti- is omitted

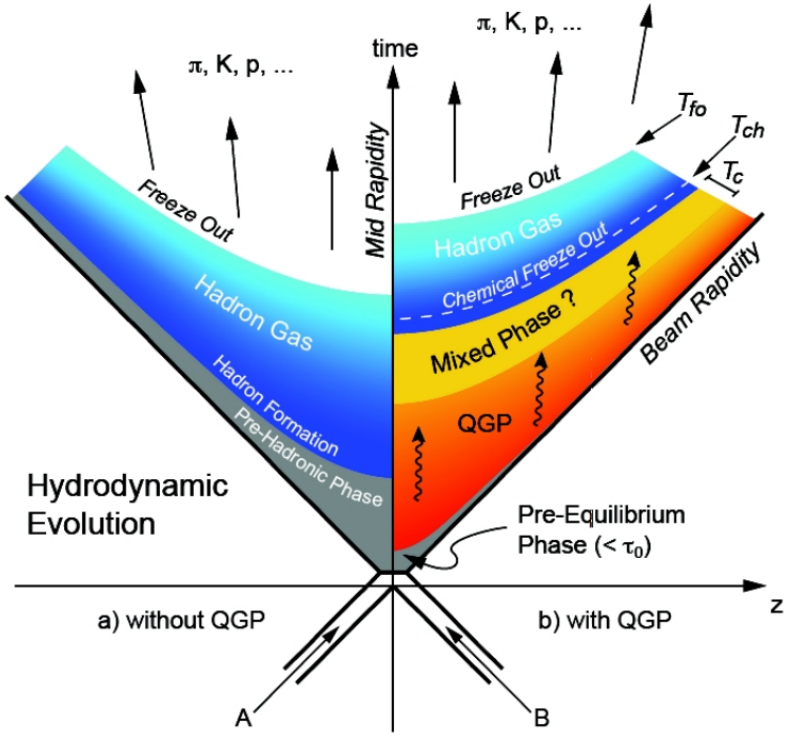

Figure 2.1 Evolution of a high-energy hadron collision in a space-time diagram. The z-direction of parallel to the beam line. The two scenarios without **(a)** and with **(b)** QGP are pointed out. Taken from [16]

2.2 Production models

2.2.1 Thermal model

The thermal model is used to describe hadron yields produced in a collision. Predictions are obtained by requiring thermodynamic equilibrium, i.e. the full occupation of the phase-space [18], and is not based on a microscopic production mechanism. The free parameters of the thermal model are the temperature T_{chem} of the system at chemical freeze-out, and the baryon chemical potential μ_{B}, which is a measure for the matter-antimatter asymmetry of the system.

The thermal model provides a realistic description of the yields of hadrons and light nuclei which can be seen in Fig. 2.2. The figure shows a comparison between particle yields measured in central (0-10%)[2] Pb–Pb collisions at $\sqrt{s_{\mathrm{NN}}} = 2.76$ TeV by ALICE alongside the predictions of the thermal model. Three different implementations of the thermal model are considered. These implementations are THERMUS, GSI-Heidelberg and SHARE 3. They differ in the list of resonances included in the calculations. Furthermore, in the SHARE model hadrons are considered to be point-like, while in the THERMUS and GSI-Heidelberg models the hadron volume is taken into account [16]. All models provide a consistent value for the temperature of the chemical freeze-out of $T_{\mathrm{chem}} = 156$ MeV.

Despite its success in reproducing measured yields, the thermal model does not provide a description about the formation of hadrons and nuclei itself. Additionally, it does not provide

[2] An explanation of centrality will be given in Sec. 4.2

an explanation how nuclei with binding energies of E ≈ 1MeV would survive in a hot environment of T ≈ 100 MeV. These are often referred to as *snowballs in hell.* For a more detailed description of the thermal model see Ref. [16].

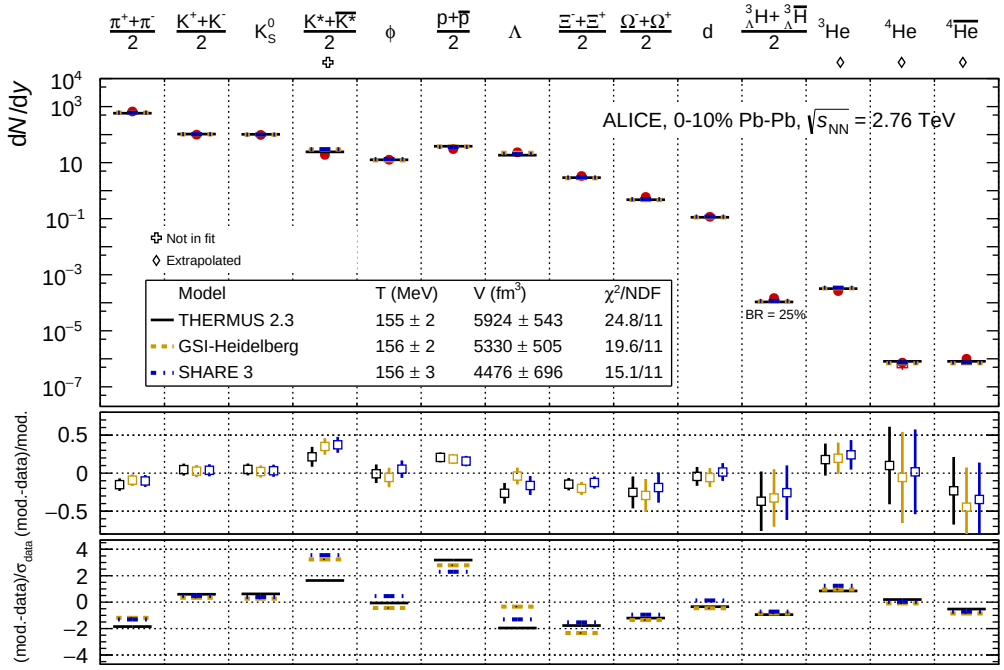

Figure 2.2 Prediction of yields of selected mesons, hadrons and (anti-)nuclei in Pb–Pb collisions at $\sqrt{s_{\mathrm{NN}}} = 2.76$ TeV by the thermal model. Taken from [19]

2.2.2 Coalescence model

Classical coalescence

The coalescence model was first proposed by Butler and Pearson [20] in 1963. It assumes that nucleons will form a nucleus if they are close in phase space. The probability to form a nucleus via coalescence is determined by the *coalescence function* $C(\sqrt{s}, \vec{k}_p, \vec{k}_n)$. This probability explicitly depends on the momenta ($\vec{k}_{p,n}$) and implicitly on their difference ($2\Delta\,\vec{k}=\vec{k}_p - \vec{k}_n$), as well as the collision energy $\sqrt{s}$. However, in first approximation it is assumed that the coalescence function does not depend on the collision energy. Closely following the derivations in [21, 22], the deuteron momentum distribution can be expressed as

$$\frac{\mathrm{d}N_\mathrm{d}}{\mathrm{d}\,\vec{k}_\mathrm{d}^{\,3}}(\sqrt{s},\vec{k}_\mathrm{d}) = \int \mathrm{d}^3\,\vec{k}_\mathrm{p}\,\mathrm{d}^3\,\vec{k}_\mathrm{n}\,\left(\frac{\mathrm{d}N_\mathrm{p,n}}{\mathrm{d}\,\vec{k}_\mathrm{p}^{\,3}\,\mathrm{d}\,\vec{k}_\mathrm{n}^{\,3}}(\sqrt{s},\vec{k}_\mathrm{p},\vec{k}_\mathrm{n})\right) C(\vec{k}_\mathrm{p},\vec{k}_\mathrm{n})\,\delta(\vec{k}_\mathrm{d}-\vec{k}_\mathrm{p}-\vec{k}_\mathrm{n}) \tag{2.1}$$

Where $\mathrm{d}N_\mathrm{p,n}$ is the number of p–n pairs in each event and the δ-function ensures momentum conservation. Momentum conservation is further discussed in Sec. 2.2.3. Transforming the momenta to $\vec{k}_\mathrm{p}^{\,*}=\vec{k}_\mathrm{d}/2+\Delta\,\vec{k}$ and $\vec{k}_\mathrm{n}^{\,*}=\vec{k}_\mathrm{d}/2-\Delta\,\vec{k}$, one obtains

$$\frac{\mathrm{d}N_\mathrm{d}}{\mathrm{d}\,\vec{k}_\mathrm{d}^{\,3}}(\sqrt{s},\vec{k}_\mathrm{d}) = \int \mathrm{d}^3\Delta\,\vec{k}\,\mathrm{d}^3\,\vec{k}_\mathrm{d}\,\left(\frac{\mathrm{d}N_\mathrm{p,n}}{\mathrm{d}\,\vec{k}_\mathrm{p}^{\,3}\,\mathrm{d}\,\vec{k}_\mathrm{n}^{\,3}}(\sqrt{s},\vec{k}_\mathrm{p}^{\,*},\vec{k}_\mathrm{n}^{\,*})\right) C(\vec{k}_\mathrm{p},\vec{k}_\mathrm{n})\,\delta(\vec{k}_\mathrm{d}-\vec{k}_\mathrm{p}-\vec{k}_\mathrm{n}) \tag{2.2}$$

Evaluating the deuteron momentum integral:

$$\frac{\mathrm{d}N_\mathrm{d}}{\mathrm{d}\,\vec{k}_\mathrm{d}^3}(\sqrt{s},\vec{k}_\mathrm{d}) = \int \mathrm{d}^3\Delta\,\vec{k}\,\left(\frac{\mathrm{d}N_\mathrm{p,n}}{\mathrm{d}\,\vec{k}_\mathrm{p}^3\,\mathrm{d}\,\vec{k}_\mathrm{n}^3}(\sqrt{s},\vec{k}_\mathrm{p}^*,\vec{k}_\mathrm{n}^*)\right) C(\vec{k}_\mathrm{p},\vec{k}_\mathrm{n}) \tag{2.3}$$

In this model, the relative momentum $\Delta\,\vec{k}$ is supposed to be small compared to the total momentum ($|\Delta\,\vec{k}| \ll |\,\vec{k}_\mathrm{d}\,|$). With this approximation, the Lorentz-invariant form of Eq. 2.3 becomes:

$$\gamma_\mathrm{d}\left(\frac{\mathrm{d}N_\mathrm{d}}{\mathrm{d}\,\vec{k}_\mathrm{d}^3}\right)(\sqrt{s},\vec{k}_\mathrm{d}) \approx \left[\frac{\gamma_\mathrm{d}}{\gamma_\mathrm{p}\gamma_\mathrm{n}}\int \mathrm{d}^3\Delta\,\vec{k}\;\; C(\Delta\,\vec{k})\right] \times \gamma_\mathrm{p}\gamma_\mathrm{n}\left(\frac{\mathrm{d}N_\mathrm{p,n}}{\mathrm{d}\,\vec{k}_\mathrm{p}^3\,\mathrm{d}\,\vec{k}_\mathrm{n}^3}(\sqrt{s},\vec{k}_\mathrm{d}\,/2,\vec{k}_\mathrm{d}\,/2)\right) \tag{2.4}$$

Finally, the coalescence function is approximated with a step function ($\Theta(\Delta k^2 - p_0^2)$), where p_0 is the so called *coalescence momentum*. This means that the coalescence probability is zero, if the relative momentum $|\Delta\,\vec{k}\,|$ of the proton-neutron pair is larger than p_0 and one, if it is smaller. This is called the *spherical approximation*. This approximation allows to evaluate the integral within the brackets:

$$\gamma_\mathrm{d}\left(\frac{\mathrm{d}N_\mathrm{d}}{\mathrm{d}\,\vec{k}_\mathrm{d}^3}\right)(\sqrt{s},\vec{k}_\mathrm{d}) \approx \left[\frac{4\pi p_0^3}{3}\right] \times \gamma_\mathrm{p}\gamma_\mathrm{n}\left(\frac{\mathrm{d}N_\mathrm{p,n}}{\mathrm{d}\,\vec{k}_\mathrm{p}^3\,\mathrm{d}\,\vec{k}_\mathrm{n}^3}(\sqrt{s},\vec{k}_\mathrm{p}{=}\vec{k}_\mathrm{d}\,/2,\vec{k}_\mathrm{n}{=}\vec{k}_\mathrm{d}\,/2)\right) \tag{2.5}$$

Eq. 2.5 shows that, if the relative momentum of the proton-neutron pair is within the volume of a sphere with radius p_0 ($V = \frac{4\pi}{3}p_0^3$) in momentum space, the nucleons form a deuteron. This model is very successful in reproducing measurements of nuclei produced in small systems (e.g. e^+e^- and pp), but since it does not take spatial correlations into account, it needs to be modified to describe coalescence in larger systems (e.g. Pb–Pb, Au–Au). In this modified model, the coalescence condition is not fulfilled when the nucleons lie within a sphere with radius p_0 in momentum space but only if they also lie within a sphere with radius r_0 in real space. This condition is always met in small systems, because the size of the emission source is always smaller than the size of the deuteron. In this model, the quantum-mechanical aspects of the interaction are not considered.

A model that works on a quantum mechanical[3] basis was proposed by Scheibl and Heinz [23] in 1999 and it is based on the Wigner function [24] of the deuteron. It is further discussed later in this Chapter.

In order to solve Eq. 2.5, one can employ two different approaches. One option is to determine $\frac{\mathrm{d}N_\mathrm{p,n}}{\mathrm{d}\,\vec{k}_\mathrm{p}^3\mathrm{d}\,\vec{k}_\mathrm{n}^3}$ using a Monte Carlo simulation or by following an analytical approach. The analytical approach is based on the assumption that the proton and the neutron momentum distributions are uncorrelated and thus the combined distribution can be factorized as:

$$\frac{\mathrm{d}N_\mathrm{p,n}}{\mathrm{d}\,\vec{k}_\mathrm{p}^3\,\mathrm{d}\,\vec{k}_\mathrm{n}^3} = \frac{\mathrm{d}N_\mathrm{p}}{\mathrm{d}\,\vec{k}_\mathrm{p}^3}\frac{\mathrm{d}N_\mathrm{n}}{\mathrm{d}\,\vec{k}_\mathrm{n}^3} \tag{2.6}$$

However, this is only an approximation. For example, at energies close to the antideuteron production threshold ($\sqrt{s} \approx 6m_\mathrm{p}$)[4], the production of multiple antiparticles is suppressed

[3] The model used here is more semi-classical than purely quantum mechanical

[4] in order to produce an antideuteron, one antineutron and one antiproton need to be produced. In a pp collision this leads to p+p→ p+p+p+$\bar{\mathrm{p}}$+n+$\bar{\mathrm{n}}$, so the final state requires 6 nucleons.

compared to uncorrelated production [25]. This means that by using this approach, the predicted deuteron yields overestimate the true yields at low energies.
A further possible simplification is to equate proton and neutron yields. This gives an invariant deuteron yield of:

$$E_{\mathrm{d}}\frac{\mathrm{d}N_{\mathrm{d}}}{\mathrm{d}\,\vec{k}_{\mathrm{d}}^{3}} \approx B_2\left(E_{\mathrm{p}}\frac{\mathrm{d}N_{\mathrm{p}}}{\mathrm{d}\,\vec{k}_{\mathrm{p}}^{3}}\right)^2 \tag{2.7}$$

B_2 is the so called *coalescence parameter*, which can be expressed as

$$B_2 = \frac{4\pi p_0^3}{3}\frac{m_{\mathrm{d}}}{m_{\mathrm{p}}^2} \tag{2.8}$$

In the Monte Carlo approach, the full phase-space distribution, as well as the yields and the correlated production of nuclei, can be taken directly from the event generator. With this approach, it is possible to solve Eq. 2.5 without any further approximations. The only problem is that event generators are known to not perfectly describe nature. For this reason, the goal of this thesis is to tune an event generator (namely EPOS 3) to reproduce (anti)proton[5] data in the desired energy range so that $\frac{\mathrm{d}N_{\mathrm{p,n}}}{\mathrm{d}\,\vec{k}_{\mathrm{p}}^{3}\mathrm{d}\,\vec{k}_{\mathrm{n}}^{3}}$ can be determined properly.
Results of the Monte Carlo coalescence with spherical approximation and using the Wigner function are presented in Sec. 5.

Coalescence using the Wigner function

The idea to use the Wigner function of the deuteron to explain their formation was first published by Scheibl and Heinz [23] in 1999. The Wigner function of an object is defined as

$$W(x,p) = \frac{1}{\pi\hbar}\int_{-\infty}^{\infty}\psi^*(x+y)\psi(x+y)e^{2ipy/\hbar}\mathrm{d}y \tag{2.9}$$

where $\psi(x)$ is the wave function of the object of interest, in this case the deuteron. The Wigner function gives the probability of a deuteron to exist with a certain relative momentum and distance between its constituents.
The derivation of the deuteron production spectra is given in the following [26]:
Consider a proton and a neutron in a frame of reference where their center of mass is moving non-relativistic. The deuteron yield $\frac{\mathrm{d}N_{\mathrm{d}}}{\mathrm{d}P_{\mathrm{d}}}$ can be expressed by projecting the deuteron density matrix ρ_{d} onto the two-nucleon density matrix ρ_{pn}

$$\frac{\mathrm{d}^3N_{\mathrm{d}}}{\mathrm{d}P_{\mathrm{d}}^3} = \mathrm{tr}(\rho_{\mathrm{d}}\rho_{\mathrm{pn}}) \tag{2.10}$$

where ρ_{d} describes a pure state $|\phi_{\mathrm{d}}\rangle\langle\phi_{\mathrm{d}}|$ and ρ_{pn} can be expressed as $\rho_{\mathrm{pn}} = |\psi_{\mathrm{p}}\psi_{\mathrm{n}}\rangle\langle\psi_{\mathrm{n}}\psi_{\mathrm{p}}|$, the normalization being $\langle\psi_{\mathrm{n}}\psi_{\mathrm{p}}|\psi_{\mathrm{p}}\psi_{\mathrm{n}}\rangle = N_{\mathrm{p}}N_{\mathrm{n}}$ with N_{p} and N_{n} being the average multiplicities of protons and neutrons per event, respectively.

[5] and (anti)neutron. Since there is very little data on antineutrons perfect isospin symmetry is assumed

Evaluating the trace in Eq. 2.10 one finds

$$\frac{\mathrm{d}^3N_\mathrm{d}}{\mathrm{d}P_\mathrm{d}} = S\int \mathrm{d}^3x_1\mathrm{d}^3x_2\mathrm{d}^3x_1'\mathrm{d}^3x_2'\phi_\mathrm{d}^*(x_1,x_2)\phi_\mathrm{d}(x_1',x_2')\left\langle\psi_\mathrm{n}^\dagger(x_2')\psi_\mathrm{p}^\dagger(x_1')\psi_\mathrm{p}(x_1)\psi_\mathrm{n}(x_2)\right\rangle \tag{2.11}$$

where S=3/8 is a factor taking spin and isospin statistics into account. The deuteron wave function can be factorized as a plane wave describing the motion of the center of mass with momentum P_d and an internal wave function φ_d

$$\phi_\mathrm{d}(x_1,x_2) = (2\pi)^{-3/2}\exp\{iP_\mathrm{d}\cdot(x_1+x_2)/2\}\varphi_\mathrm{d}(x_1-x_2) \tag{2.12}$$

and the two-nucleon density ρ_pn is replaced with the two-body Wigner function W_np

$$\left\langle\psi_\mathrm{n}^\dagger(x_2')\psi_\mathrm{p}^\dagger(x_1')\psi_\mathrm{p}(x_1)\psi_\mathrm{n}(x_2)\right\rangle = \int\frac{\mathrm{d}^3p_\mathrm{n}}{(2\pi)^3}\frac{\mathrm{d}^3p_\mathrm{p}}{(2\pi)^3}W_\mathrm{np}\left(p_\mathrm{n},p_\mathrm{n},\frac{x_2+x_2'}{2},\frac{x_1+x_1'}{2}\right)$$
$$\times\exp[ip_\mathrm{n}(x_2-x_2')]\exp[ip_\mathrm{p}(x_1-x_1')]. \tag{2.13}$$

Using the coordinate transformations $r_\mathrm{p}=(x_1+x_1')/2$, $r_\mathrm{n}=(x_1+x_1')/2$, $r=r_\mathrm{n}-r_\mathrm{p}$, $\zeta=x_1-x_1'-x_2+x_2'$, $\rho=(x_1-x_1'+x_2-x_2')$ and $p=p_\mathrm{n}+p_\mathrm{p}$, $q=(p_\mathrm{n}-p_\mathrm{p})/2$ as well as Eq. 2.13 and Eq. 2.12 in Eq. 2.11 one obtains

$$\frac{\mathrm{d}^3N_\mathrm{d}}{\mathrm{d}P_\mathrm{d}} = \frac{S}{(2\pi)^6}\int\mathrm{d}^3q\int\mathrm{d}^3r_\mathrm{p}\mathrm{d}^3r_\mathrm{n}\mathscr{D}(r,q)W_\mathrm{np}(P_\mathrm{d}/2+q,P_\mathrm{d}/2-q,r_\mathrm{n},r_\mathrm{p}) \tag{2.14}$$

where $\mathscr{D}(r,p)$ is the Wigner function as defined in Eq. 2.9. Assuming a Gaussian internal wave function for the deuteron

$$\varphi(r) = (\pi d^2)^{-3/4}\exp\left(-\frac{r^2}{2d^2}\right) \tag{2.15}$$

the corresponding Wigner function is

$$\mathscr{D}(r,q) = 8\mathrm{e}^{-r^2/d^2-q^2d^2}, \tag{2.16}$$

where d=3.2 fm is the characteristic size parameter of the deuteron wave function. W_np can be factorized into a momentum ($G_\mathrm{np}(P_\mathrm{d}/2+q,P_\mathrm{d}/2-q)$) and a coordinate dependent ($H_\mathrm{np}(r_\mathrm{n},r_\mathrm{p}) = h(r_\mathrm{n})\cdot h(r_\mathrm{p})$) function. If the spatial distribution of protons and neutrons are assumed to be uncorrelated one can choose a Gaussian ansatz for them

$$h(r) = (2\pi\sigma^2)^{-3/2}\exp\left(-\frac{r^2}{2\sigma^2}\right). \tag{2.17}$$

With these assumptions Eq. 2.14 can be rewritten as

$$\frac{\mathrm{d}^3N_\mathrm{d}}{\mathrm{d}P_\mathrm{d}} = \frac{S\zeta}{(2\pi)^6}\int\mathrm{d}^3q\ 8\ \mathrm{e}^{-q^2d^2}G_\mathrm{np}(P_\mathrm{d}/2+q,P_\mathrm{d}/2-q), \tag{2.18}$$

where the factor

$$\zeta = \left(\frac{d^2}{d^2+4\sigma^2}\right)^{3/2} \tag{2.19}$$

depends on the size of the nucleon emission source σ. Eq. 2.18 describes the formation of a deuteron from a given proton-neutron pair with relative momentum $2q$ in their center of mass frame, with a probability of

$$w = S\,\zeta\,8\mathrm{e}^{-q^2d^2} \tag{2.20}$$

This approach gives a coalescence probability that depends on the distance and the relative momentum of the neutron-proton pair, without any free parameter which would need to be determined by fitting to an existing dataset.

2.2.3 Problems of the coalescence model

The value of the coalescence momentum

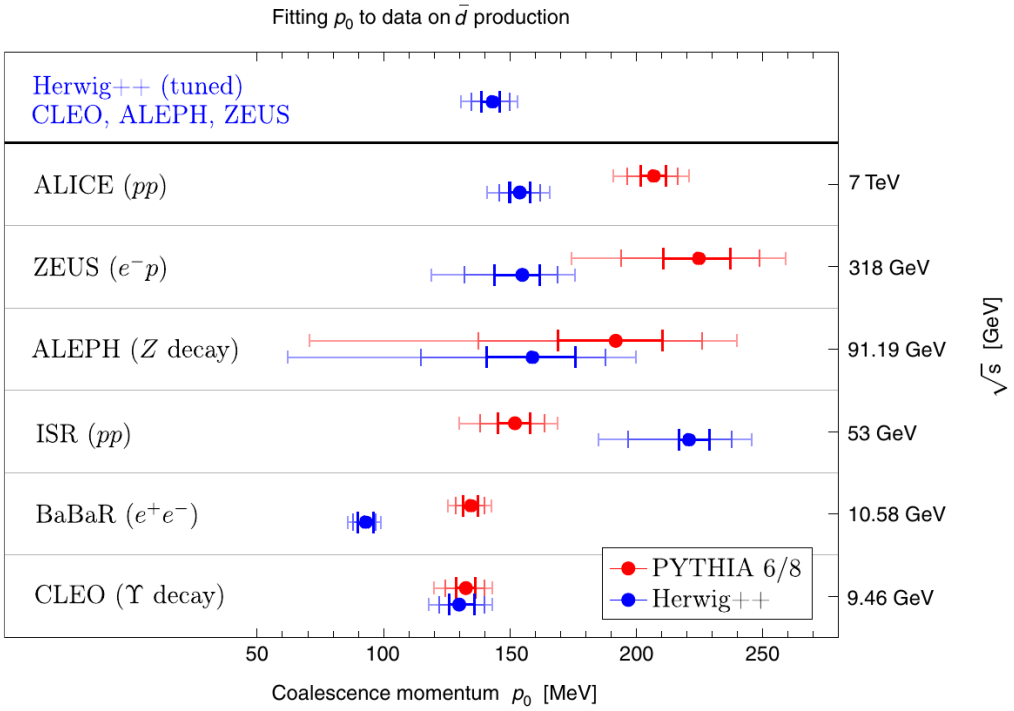

Figure 2.3 Coalescence momentum p_0 obtained from a fit to different datasets. Taken from [27].

In order to obtain the coalescence momentum p_0 and the distance r_0 they must be fit to an existing dataset using an event generator. Fig. 2.3 shows the results of fitting the event generators PYTHIA 6/8 [28] and Herwig++ [29]. The experimental data ranges from low energies ($\sqrt{s}$ ~9 GeV) to LHC energies ($\sqrt{s} = 7$ TeV) and from small sources (e^+e^-) to medium sized sources (pp). Because of this, the fit was performed using only the coalescence momentum. Notably, the coalescence momentum varies between 90 and 220 MeV/c even using the same event generator and with a nontrivial relation to the collision energy. The reason is that the p_0 parameter is not a physical observable, but rather a fit parameter which includes the effects of different variables and model assumptions. Such assumptions might be, for example, whether the model includes nuclei from weak and strong decays or if it includes spin-isospin statistics. These effects cause the coalescence momentum to depend on the system size and

the collision energy. This means that the spherical approximation requires fitting p_0 and r_0 for each colliding system separately.

Momentum conservation

When the coalescence model was first proposed, it was criticized because it either requires a third particle or it breaks energy and momentum conservation:

$$k_{\mathrm{np}}^2 = \frac{1}{4m_{\mathrm{d}}^2}[(m_{\mathrm{d}}^2 - m_{\mathrm{n}}^2 - m_{\mathrm{p}}^2)^2 - 4m_{\mathrm{p}}^2 m_{\mathrm{n}}^2] \tag{2.21}$$

$$\text{(with: } m_{\mathrm{p}} \approx m_{\mathrm{n}}\text{)} \quad \approx \frac{1}{4m_{\mathrm{d}}^2}[m_{\mathrm{d}}^4 + \cancel{2m_{\mathrm{p}}^4} - 4m_{\mathrm{d}}^2 m_{\mathrm{p}}^2 + \cancel{2m_{\mathrm{p}}^4} - \cancel{4m_{\mathrm{p}}^4}] \tag{2.22}$$

$$= \frac{1}{4m_{\mathrm{d}}^2}[m_{\mathrm{d}}^2(m_{\mathrm{d}}^2 - \underbrace{(m_{\mathrm{p}} + m_{\mathrm{n}})^2}_{>m_{\mathrm{d}}^2}] < 0, \tag{2.23}$$

where k_{np} is the relative momentum between the proton and the neutron. The deuteron mass relates to the proton and neutron mass as $m_{\mathrm{d}} < m_{\mathrm{p}} + m_{\mathrm{n}}$. This problem can be solved in different ways. Firstly, since the binding energy of the deuteron is only 2.2 MeV, the effect is small compared to the mass of the nucleons. This means that if one of the nucleons (or both) is even slightly off-shell, and thus the masses relate as $m_{\mathrm{d}} \geq m_{\mathrm{p}} + m_{\mathrm{n}}$, the energy-momentum relation can be restored again:

$$k_{\mathrm{np}}^2 = \frac{1}{4m_{\mathrm{d}}^2}[m_{\mathrm{d}}^2(m_{\mathrm{d}}^2 - \underbrace{(m_{\mathrm{p}} + m_{\mathrm{n}})^2}_{\leq m_{\mathrm{d}}^2}] \geq 0 \tag{2.24}$$

The larger the difference between the mass of the nucleus and the sum of the masses of the nucleons, the larger the allowed momentum.
A result of this solution is that it excludes all nucleons from decays from coalescence. This fraction makes up around 65% [30] of all nucleons. Another possible solution of the problem can be found in Heisenbergs uncertainty principle. If the emission source of nucleons has a size of R, then the momentum uncertainty can be evaluated as:

$$\Delta r \cdot \Delta p \geq \frac{1}{2} \tag{2.25}$$

$$\Delta p \geq \frac{1}{2R}, \tag{2.26}$$

where natural units ($\hbar$=c=1) are used. If one assumes a source size of 1 fm, which is a common value for the system size in pp collisions, the uncertainty on the momentum is 100 MeV/c. If the source size is around 7 fm, which is a common value for heavy-ion collisions, the uncertainty is still around 14 MeV/c, enough to account for the binding energy of a deuteron. Relying on this assumption, nucleons from strong decays can form nuclei, which increases the source size by less than 1 fm [30]. For the coalescence studies in this thesis, the latter model is used and nucleons from strong decays can form a nucleus via coalescence.

2.2.4 Comparison of coalescence and thermal model

The production mechanism of light nuclei in hadron collisions is still debated. It is not clear whether we have a thermal production or whether nuclei are produced from coalescence. A valuable test for these models is hypertriton production due to its large radius of 7-14 fm, compared to 2.15 fm for regular triton and 2.48 fm for ^{3}He. Hypertriton is a nucleus consisting of a proton, a neutron and a Λ baryon. Recent results by the ALICE Collaboration [31] seem to favor coalescence over the thermal model. They measured the S_3 observable, which is the ratio between the yields $S_3 = \frac{^3_\Lambda\mathrm{H}}{(^3\mathrm{He}\times\frac{\Lambda}{p})}$ of hypertriton and ^{3}He. This observable is sensitive to the formation mechanism, since the thermal model does not take the size of the produced nucleus into account, while the coalescence model does. This means that the predictions by the thermal model and the coalescence model are very different at low multiplicities. The predictions of both models and recent results by ALICE in pp HM, p–Pb and Pb–Pb can be seen in Fig. 2.4. The measurement by ALICE in pp and p–Pb collisions favor a 2-body coalescence model, i.e. ^{3}He (H_Λ) form by coalescence between a deuteron and a proton (Λ). With the help of the Run 3 data, the ALICE collaboration plans to comprehensively solve this puzzle.

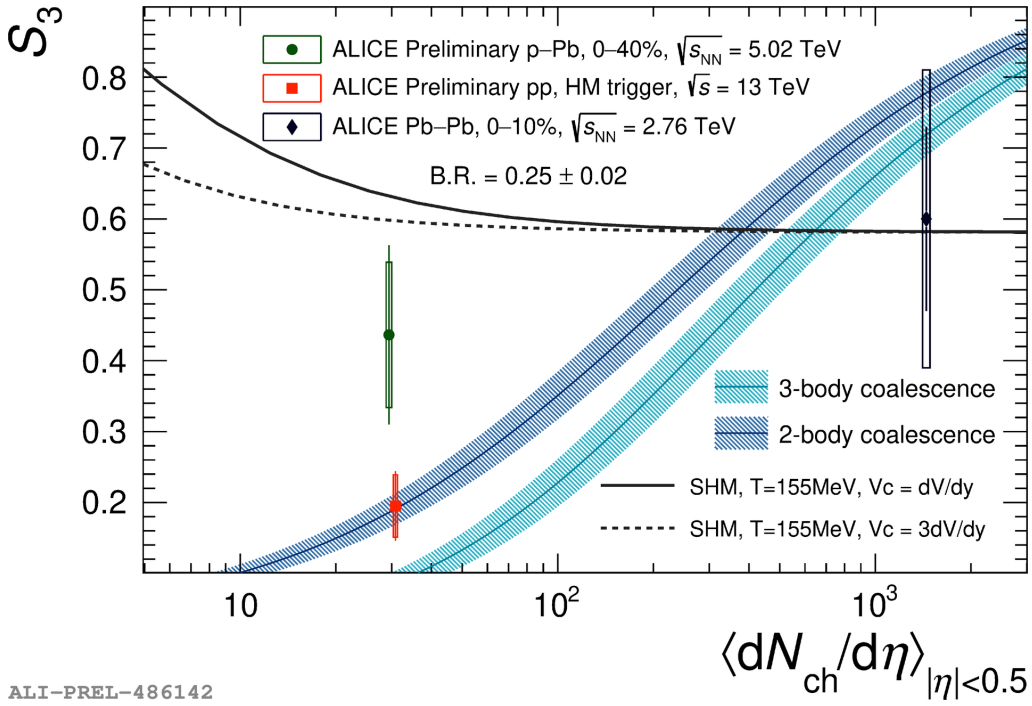

Figure 2.4 The S_3 observable as predicted by the coalescence model and by the thermal model, alongside results by ALICE in pp HM, p–Pb and Pb–Pb collisions. Taken from [31]

2.3 Existing antideuteron cosmic ray predictions

As discussed in Sec. 1, constraining the antideuteron flux is of utmost importance for dark matter predictions. Indeed, many attempts have been made to constrain the expected secondary antideuteron flux at earth and to model the expected signal from dark matter. These

predictions are mainly made using the spherical approximation [15, 27], but the first results using the Wigner function approach have recently been published [32].

Fig. 1.3 shows the prediction for antideuterons obtained from an analytical spherical approximation coalescence model with coalescence momenta $p_0 = 160$ MeV/c and $p_0 = 248$ MeV/c [15][6]. In this paper, the authors use a parameterization developed in [33] to model their antiproton spectra. While these parameterizations are fitted to multiple experimental datasets, even the authors of [33] admit that the systematic uncertainties introduced with these parameterizations range from 10% at intermediate collision energy (few GeV - 100 GeV) up to 50% at TeV energies.

Fig. 2.5 shows the predictions of the secondary antideuteron flux and the dark matter in-

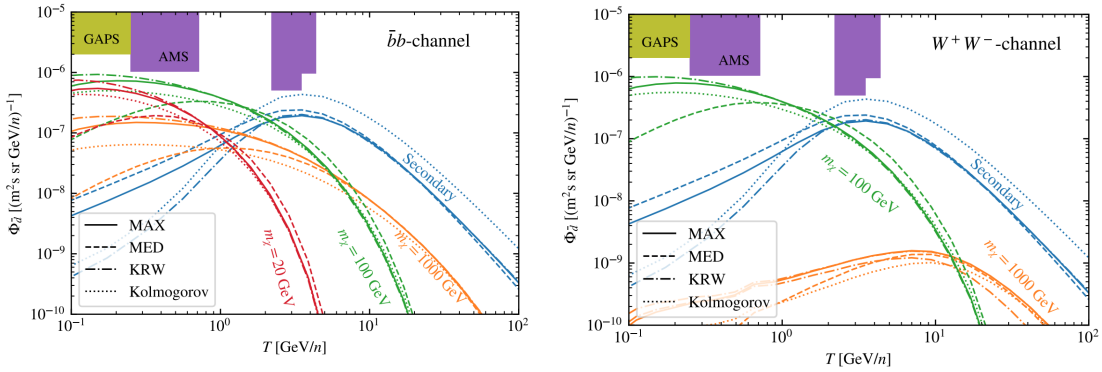

Figure 2.5 Antideuteron flux for secondaries at earth and the potential dark matter signal for different dark matter masses ranging from $m_\chi = 20$ GeV to 1 TeV. The left panel shows the predictions for the annihilation of dark matter into $b\bar{b}$ and the right panel shows annihilation into W^+W^-. Both predictions use the MED and MAX propagation parameters from [11] as well as a parameterization developed by Kappl, Reinert und Winkler (KRW) [34] and their own parameterization inspired by a Kolmogorov diffusion model. Solar modulation is modeled using a force-field approximation, with $\phi = 600$ MV. The predictions are compared to GAPS [14] and AMS-02 [13] sensitivities. Both predictions are obtained using a Wigner function based analytical coalescence model. Taken from [32].

duced primary flux at earth. The predictions for primaries are made for multiple dark matter masses ($m_\chi = 20$, 100 and 1000 GeV), as well as for two different annihilation channels ($b\bar{b}$ and W^+W^-). The results are shown for different propagation models (MED,MAX from [11], KRW from [34] and their own model based on Kolmogorov diffusion). The authors use a Wigner function based analytical coalescence model and use QGSJET-II for their antiproton input. Since no antideuteron was ever detected in cosmic rays, it is hard to gauge the quality of these predictions. However, it is clear that the uncertainties on these predictions a substantial.

[6] In the original paper the authors wrote GeV, which would be 3 orders of magnitude larger than usual values.

Chapter 3

The EPOS event generator

All following predictions will be made using the EPOS 3.117 event generator. An event generator is a program used to simulate the collisions of particles. EPOS [35] stands for **E**nergy conserving quantum mechanical approach, based on **P**artons, parton ladders, strings, **O**ff-shell remnants, and **S**plitting of parton ladders. Its most important features are the implementation of multiple scattering of partons, the inclusion of collective effects and hydrodynamic evolution of the initial state. EPOS 3 was specifically developed to explain heavy ion collisions at LHC energies. A short overview of the functionalities will be given in the following.

3.1 Working principle of EPOS

In EPOS, the colliding particles are divided into target and projectile. Initially, all nucleons of the target and the projectile are distributed using the Woods-Saxon potential [36]. The interaction between nucleons is described using pomerons. For each interacting nucleon pair, one pomeron is placed between them. The pomeron was initially postulated to explain the slowly rising cross section in interactions between hadrons at high energies [37]. It is based on the Regge-theory, which is used inside EPOS to model the interactions between hadrons [38]. In EPOS, pomerons are modeled by parton ladders. This mechanism can be seen in Fig. 3.1. The interaction between two particles is modeled by the exchange of (sometimes multiple) parton ladders. Each of these parton ladders creates new partons which bind together to so-called strings.
Each string is created between two (di-)quarks emerging from these parton ladders. The strings then break up via the Schwinger mechanism depicted in Fig. 3.2 and form hadrons. The breakup of the string into $q\bar{q}$ pairs as well as $dq\overline{dq}$ (diquark-antidiquark) pairs. Diquarks are objects composed of two quarks which are not color neutral, unlike mesons. Fragmentation points with diquarks form baryons, the others form mesons. The created hadrons can be in excited states, for example $N^*(1440)$ instead of protons. This mechanism implicitly conserves baryon number and electric charge.
Each fragment is assigned a transverse momentum. If the transverse momentum of a particle is high, it will be part of the so called corona while fragments with low p_T will be part of the core. The core is the part that constitutes the quark-gluon plasma (QGP). In the QGP string fragments are dissolved into a bulk matter, which evolves using hydrodynamics (HYDRO). The bulk matter expands during its evolution, decreasing the temperature and the density. When

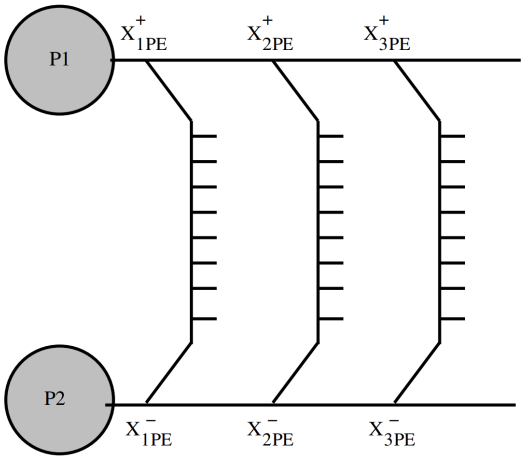

Figure 3.1 A scheme of an event with multiple interactions. Several ladders are exchanged in parallel. All ladders exist at the same time. The total energy is shared between ladders. This means that it's impossible to have an infinite number of ladder. The total energy is conserved. x_{PE} refers to the fraction of the total momentum the ladder receives. Taken from [39].

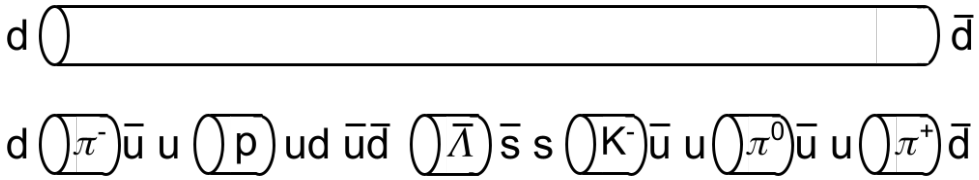

Figure 3.2 String fragmentation and hadron formation via the Schwinger Mechanism. The string between a $d\,\overline{d}$ pair breaks into multiple $q\,\overline{q}$ and $d\,q\,\overline{d\,q}$ pairs.

density and temperature reach a critical value, the bulk matter hadronizes. In nature this is a two-step process. First, the QGP reaches the critical temperature T_{c} and undergoes a phase transition to a gas of strongly interacting hadrons. The particles in the gas scatter both elastically and inelastically. The gas keeps expanding and its temperature decreases, leading to the chemical freeze-out (see Sec. 2.1). Fragments which escape the core and make it into the corona further create jets or hadrons. After the chemical freeze-out all particles, from core and corona, undergo final-state interactions, such as rescattering. This is the hadronic cascade (HACAS) and it is handled by the UrQMD [40] model. The system keeps expanding, the temperature decreasing and eventually the kinetic freeze-out occurs (see Sec. 2.1). After this point, only weakly-decaying particles or final-state particles exist.

3.2 EPOS event output

The most important feature of EPOS is the fact that it performs the full simulation of the entire event. This means that all resonances and intermediate particles can be accessed, even if they do not directly contribute to the final state. For each of these particles, the position and the momentum at their creation is stored. To differentiate between particles at intermediate

stages of the system evolution and the final state, multiple flags are used in the output of EPOS. A selection of flags and a short description can be seen in Tab. 3.1. Each flag can have different purposes at different stages. Their meaning will be discussed for each stage of the event separately. Additionally to the flags, each particle has an internal index attached to it. The index is not directly stored, but it can be retrieved by the order in which the particles are stored in the output. This means that the first particle in the output has index 1 and so forth. This index is important to connect the mother and daughter particles in decays.

Name	Values	Description
id	-1120, -1220,...	particle ID according to ISAJET convention [41]
ist	-2, -1, 0, 1, 3, 6, 7, 8, 21, 29, 31	Status variable. Serves a multitude of purposes
ior/jor	>=0	Mother particle. 0 if particle is primary.
zus	-999, -2, 0, >0	Mother particle if $geq0$, special purposes for < 0
x,y,z,t	various	Four position. Units are fm (c=1)
px,py,pz,en	various	Four momentum. Units are GeV
bim	>=0	impact parameter or amount of pomerons

Table 3.1 Selection of flags associated with every particle in EPOS. Possible values and a short description are given. Flags often serve multiple purposes.

Before discussing the existing flags, it is important to note that EPOS 3 has different settings for its simulation. Two important functionalities of EPOS are HYDRO and HACAS. By applying both HYDRO and HACAS, the full functionality of EPOS is used. The initial state is evolved using hydrodynamics on the core until the chemical freeze-out. After that, the final-state interactions are modeled using the UrQMD[40] model until they reach the kinetic freeze-out. When turning off HACAS, the particles after HYDRO are no longer interacting and chemical and kinetic freeze-out coincide. This is often used to model pp collisions, as it saves computation time. Since the system in pp is not as dense as in heavy-ion collisions, kinetic freeze-out is achieved shortly after chemical freeze-out. Therefore, turning off HACAS has only a small influence on the predictions. The third option is to disable both HYDRO and HACAS. This turns off the whole evolution beyond the initial state and allows to study the effect of initial anisotropies on the final state. This is often used for flow studies [42].
For antimatter production studies, mainly the first two options are used. A schematic overview of the structure of the output for both is shown in Fig. 3.3. Most of the stages are common between the two. For both, the first particles stored in the output are the projectile and the target particles. They can be differentiated by their z position. The projectile starts in negative z direction and the target in positive z direction. The target and the projectile are offset in the x direction by half of the impact parameter each. A short definition of the impact parameter is given in Sec. 4.2. In App. B a way to obtain the impact parameter of an event is explained. As mentioned above, for collisions between nuclei the nucleons are distributed according to the Woods-Saxon potential. In the EPOS output, these particles have the flag $zus = -2$ and z-coordinates far away ($\mathcal{O}(10^{15})$m) from the origin, defined by the collision point. They are assigned a value $ist = 1$, if they are participants, meaning that they interact with another nucleon, and $ist = 0$, if they are spectators, meaning they do not interact with another particle.
In the next section in the EPOS output are the parton ladders. Their *id* is always a 7 digit num-

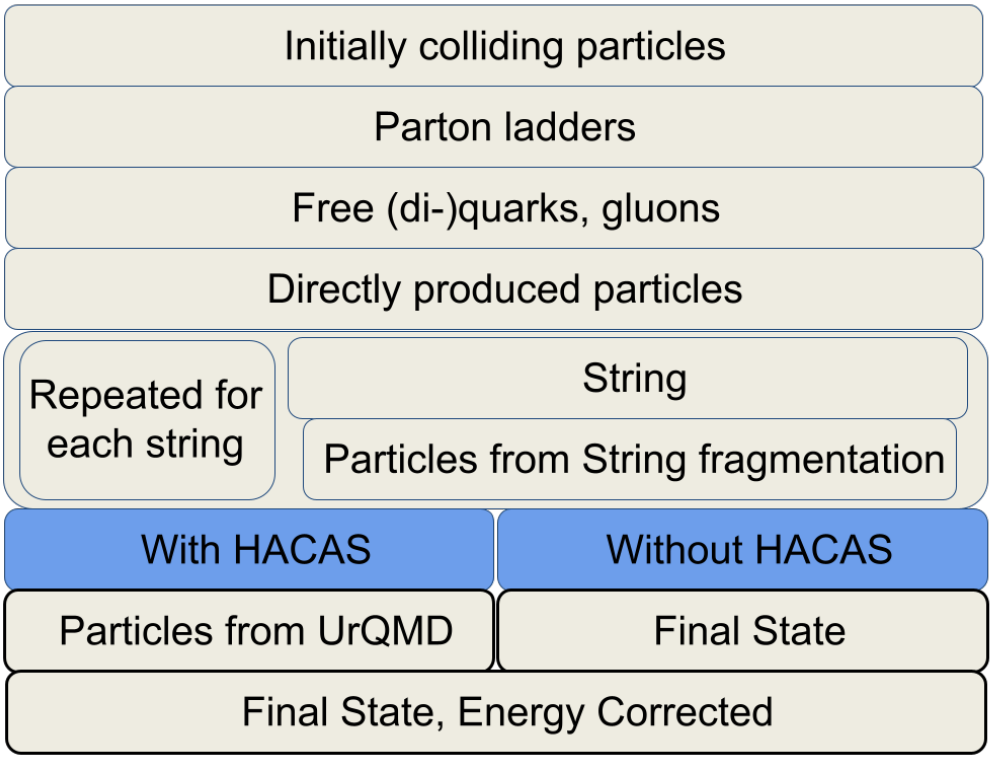

Figure 3.3 Schematic overview of the stages of EPOS output

ber ending in *99*. They have flags *zus*= 0 and *ist*= 31. *ior* and *jor* correspond to the indices of the two nucleons that have created the parton ladder in the interaction.
Next in the output are (di)quarks and gluons created from the parton ladders. They have *zus*= 0 and *ist*= 21/25. *ist*= 25 means that the parton interacts in this step (mostly by gluon emission), while *ist*= 21 means it no longer interacts in this step. They have *ior* corresponding to the index of the parton ladder from which they originated and *jor* corresponding to the index of the parton that emitted them, if they originate from an *ist*= 25 parton. Otherwise *jor*= 0.
Afterwards, a list of directly created particles (mostly highly excited resonances like $N^*(1665)$) is given. They have *zus*= 0, *ior*= 0 and *ist*= 3/7. *ist*= 3 means that the particle is being directed to the HACAS, *ist*= 7 that it is part of the core and of the hydrodynamic evolution. If HACAS is disabled, particles with *ist*= 3 will be assigned *ist*= 1.
In the next block are strings and their fragments. The *id* of a string is a 9 digit number starting with an 8. The following four digits stand for the number of up, down, strange and charm quarks. The subsequent four digits for their antiparticles. This means 800201010 represents an object with two strange quarks, one anti-up and one anti-strange quark. The fragments of a string are recorded immediatly after the corresponding string in the output. This structure is repeated for each string. Strings have *zus*= 0, *ist*= 29. *ior* and *jor* correspond to the two (di-)quarks in the list of free quarks which make up this string. The fragments also have *zus*= 0, but have *ist*= 3/7 depending on whether they are being directed to HACAS (3) or HYDRO (7).
Next in the output, there are all particles after HYDRO has finished. This section consists of all

particles from HYDRO and from the corona. Here one has to be careful: the PID of unstable particles returned from HYDRO is not in the ISAJET convention, but the PDG convention[43]. However, their decay products are again in the ISAJET convention.
If HACAS is enabled, particles that come from strong decays will have *zus*= −999 and *ior*= 0. This is, because UrQMD does not return the mother of these particles.
If HACAS is disabled, these particles will have their mothers assigned to them with *zus* and *ior*. Particles which still can decay (long lived resonances) have *ist*= 1, stable particles have *ist*= 0. The daughter particles are listed after, with *ior* set to the mother particle. These particles with *ist*= 0 are the final-state particles measured in an experiment. If HACAS is disabled, there is no differentiation between decays from long and short-lived resonances. In addition, even if HACAS is enabled, EPOS still returns an additional set of particles as if HACAS was disabled. These particles are labeled with *zus*= 0 and *ist*= 6/8. *ist*= 6 is for particles which can still decay, 8 for stable particles.
Finally, EPOS does not entirely conserve energy. In order to account for this, an energy correction a posteriori is applied. This creates a new set of particles with *zus*= −2 *ist*= −2 and *ior*= 0. There is no way to differentiate between particles from decays and prompt particles. The effect of this correction is extremely small and in most cases negligible.[1]. All details on the theory inside EPOS can be found in [42]. Concrete examples on how to extract certain particle groups of interest can be found in Appendix B.2

[1] From personal correspondence with Klaus Werner.

Chapter 4

Tuning EPOS to antiproton data

Experiment	Reference	System	$\sqrt{s}$ [GeV]	Phase-space
NA61/Shine	[44]	pp	7.7, 8.8, 12.3, 17.3	p_T=[0,1.3] GeV/c, y=[-1,2]
NA49	[45]	pp	17.3	p_T=[0,1.5] GeV/c, x_F=[-0.05,0.4]
NA49	[46]	p–C	17.3	p_T=[0,1.9] GeV/c, x_F=[-0.2,0.3]
LHCb	[47]	p–He	110	y=[-2.8,0.2], p=[12,110] GeV/c
BRAHMS	[48]	pp	200	y=[2.9,3.0] , y=[3.25,3.35] p_T=[0.8,4.2] GeV/c
STAR	[49]	pp	200	$\|y\| \leq 0.1$, pT=[0.35,1.17]
STAR	[49]	Au–Au	200	$\|y\| \leq 0.1$, pT=[0.35,1.17]

Table 4.1 Datasets for antiprotons compared to EPOS in this thesis. $\sqrt{s}$ values for non-pp systems are given in the nucleon-nucleon frame ($\sqrt{s_{NN}}$).

The first step to study the production of antideuterons in an event generator like EPOS is to check whether the production of antiprotons and antineutrons by the same generator is in agreement with the data. Indeed, a discrepancy would negatively affect the former. In the following, existing datasets for antiproton production measurements up to a collision energy of $\sqrt{s} = 200$ GeV are presented. This limit of the collision energy is well motivated by measurements of protons in cosmic rays. Since the main production of background antiprotons are secondaries, we can measure the energy distribution of protons in cosmic rays to estimate the energy distribution of the protons producing secondary antiprotons in collisions with the interstellar medium. Fig. 4.1 shows the proton flux measured by Voyager, AMS-02 and CREAM. The spectrum peaks around $E_k = 10$ GeV and drops off exponentially towards higher energies. The highest energy measurements of protons in cosmic rays are around 20 TeV where the flux is 3 orders of magnitude lower than at the peak. In a fixed target proton proton collision with 20 TeV kinetic energy of the projectile the center of mass energy is $\sqrt{s} = 200$ GeV. This limit motivates the cut-off at $\sqrt{s} = 200$ GeV.

In Fig. 1.3, the expected secondary flux of antideuterons alongside the predictions for primary antideuteron production from dark matter annihilation is shown. The figure shows that the expected detectable signal of dark matter is for low energy antideuterons below 1 GeV per

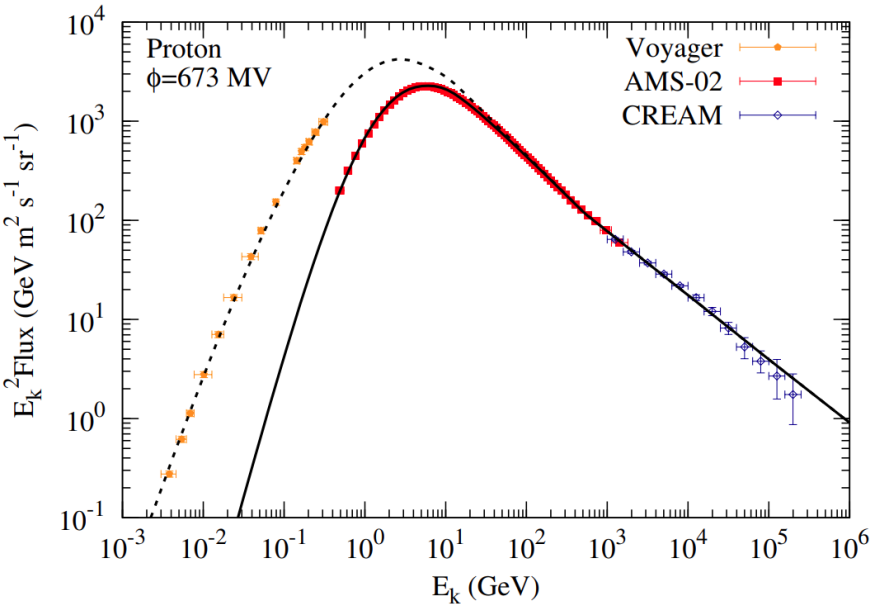

Figure 4.1 Proton flux measured by Voayager, AMS-02 and CREAM. The Voyager data is before solar modulation, while the AMS-02 and CREAM data includes it.Taken from [50].

nucleon, while the secondary background in this region is orders of magnitude lower.
Since 54% of secondary antiprotons in cosmic rays stem from pp collisions in the interstellar medium [51], the main focus is on this colliding system. The other 46% of antiprotons originates from other colliding systems, where 36% come from p–He and He–He collisions, so this colliding systems is also studied in Sec. 4.2.2. To account for the remaining 10% of antiprotons, also p–C collisions (Sec. 4.2.1) and Au–Au collisions (Sec. 4.2.3) are considered.
In Fig. 4.2 the antiproton flux as a function of the energy measured by AMS-02 is shown [52]. The lower panel shows the relative error of the flux. The figure shows that for a large energy range ($1.13 \leq E \leq 60$ GeV) the total relative error lies below 10%. This means that AMS-02 is sensitive to the contributions from collisions of heavier elements than Helium, which contribute with 10%, and as such these colliding systems also need to be studied.
In the following, a comparison between MC simulations based on EPOS and measurements is shown. For pp collisions, the MC simulations are compared with measurements by NA61 [44], NA49 [45], BRAHMS [48] and STAR [49]. For heavier colliding systems, the comparison is performed with measurements by NA49 [46], LHCb [47] and STAR [49]. Some details about these experiments are reported in Tab. 4.1.

4.1 pp collisions

4.1.1 NA61/SHINE

NA61/SHINE [44] is a fixed-target experiment located at CERN-SPS. It uses protons from a secondary hadron beam, created by colliding a proton beam with a momentum of $p = 400$ GeV/c with a beryllium target. The secondary beam is then filtered by two spectrometers for specific momenta $p = 20$, 31, 40, 80 and 158 GeV/c. These momenta correspond to $\sqrt{s} =$

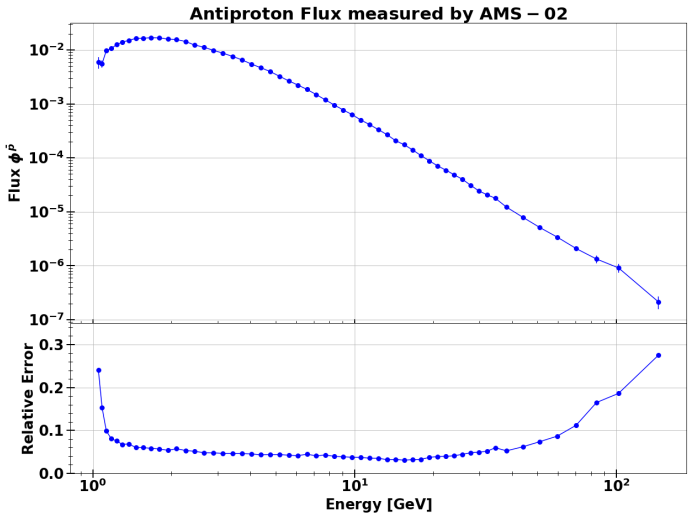

Figure 4.2 Antiproton flux near Earth measured by AMS-02 with the relative error. Taken from [52]

6.3, 7.7, 8.8, 12.3 and 17.3 GeV respectively. The secondary beam then collides with a liquid hydrogen target. They measure the differential multiplicity of antiprotons $\mathrm{d}^2N/\mathrm{d}y\mathrm{d}p_\mathrm{T}$ in the p_T range $0 \leq p_\mathrm{T} < 1.3$ GeV/c and in the rapidity range $-1 \leq y < 2$. Only for the four highest energies it has been possible to collect enough candidates to carry out the measurement. No selections on the kinematic variables are applied. The measured data and the EPOS predictions can be found in Appendix A.1. In Fig. 4.3 the ratio between the antiproton spectra simulated by EPOS and the ones measured by NA61 [44] are shown for all the center-of-mass energies. To properly assess the results, in Fig. 4.4 the rapidity distributions, obtained by integrating over the transverse momentum, are considered.

In Fig. 4.4(a), the rapidity distribution of the ratio between EPOS and NA61 for $p = 158$ GeV/c is fitted with a first-order polynomial in the rapidity range $-0.5 \leq y \leq 1.3$. The slope of the fit is 0.085 ± 0.042, showing, within 2σ, a flat behaviour of the ratio in this area. The χ^2/d.o.f (reduced χ^2) of this linear fit is 7.3. When trying to fit the whole range, the reduced χ^2 rises to 29.2 and the slope of 0.44 ± 0.09 is no longer compatible with a flat ratio. Furthermore, it is fit with an exponential function with a reduced χ^2=3.85 over the whole range. This means that EPOS overproduces the measurement exponentially more towards forward rapidities.

The rapidity distribution of the ratio between EPOS and NA61 for p=80 GeV/c can be seen in Fig. 4.4(b). It shows that EPOS produces on average 70% too many antiprotons across the whole range, with a nearly linear increase from small to large rapidity. When fitting the ratio with a first order polynomial, the slope parameter is 0.45 ± 0.07. The integrated $\mathrm{dN}/\mathrm{d}y$ yields for 40 and 31 GeV/c are shown in Fig. 4.4(c) and (d), respectively. The EPOS results do not seem to follow a clear trend, but EPOS produces a proton yield larger by a factor of 2.5 on average. The average ratio for $p = 31$ GeV/c is 1.40 ± 0.11 and for $p = 40$ GeV/c is 2.27 ± 0.12. Overall, EPOS has trouble reproducing the data measured by NA61. The production of antiprotons is too high for all collision energies considered here, especially at large rapidities.

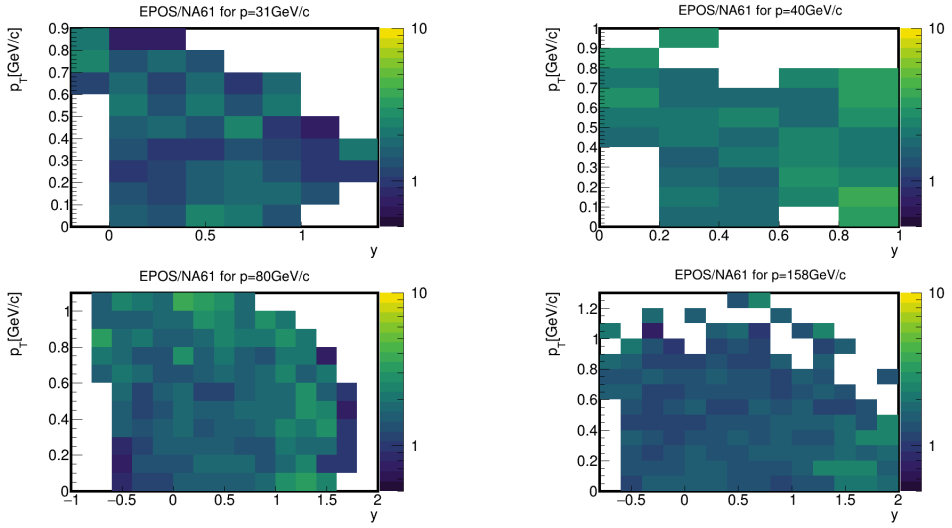

Figure 4.3 Ratio of the EPOS prediction of the differential multiplicity of antiprotons and the results of NA61. The four panels correspond to the different beam momenta of the secondary beam p=31GeV/c, p=40GeV/c, p=80GeV/c and p=158GeV/c.

4.1.2 NA49

NA49 [45] is a fixed-target experiment located at CERN's SPS. It uses a proton beam obtained with the same procedure used by the NA61 experiment. It also uses a Hydrogen target. NA49 has measured the invariant cross section for inclusive antiproton production $E\,\frac{\mathrm{d}^3\sigma}{\mathrm{d}p^3}$ at an energy of $\sqrt{s} = 17.3$ GeV as a function of Feynman-x ($x_\mathrm{F} = \frac{p_\mathrm{L}}{\sqrt{s}/2}$) and of transverse momentum p_T in the range $0 \leq p_\mathrm{T} \leq 1.5$ GeV/c and $-0.05 \leq x_\mathrm{F} \leq 0.4$. The measured cross sections and the EPOS predictions can be found in Appendix A.2.
Fig. 4.5 shows the ratio between the prediction from EPOS and the invariant cross section measured by NA49 [45]. There are three regions emerging when looking at this plot. First a "central" region ($-0.0625 \leq x_\mathrm{F} \leq 0.1625$, $0.125 \leq p_\mathrm{T} \leq 0.9$ GeV/c) in which EPOS overproduces antiprotons by around 65%, with a linear increase towards higher x_F. This can be seen in Fig. 4.6(a), which shows the p_T-integrated $\mathrm{d}\sigma/\mathrm{d}x_\mathrm{F}$ spectra. The integration is performed for $0 \leq p_\mathrm{T} \leq 1$ GeV/c. The ratio is fitted with a first order polynomial, where the slope parameter is 1.47 ± 0.25 and $\chi^2 = 2.8 \times 10^{-5}$. The reduced χ^2 for an exponential fit over this region is $\chi^2/\mathrm{d.o.f} = 2.9 \times 10^{-5}$, slightly worse than the linear fit. Both reduced χ^2 are very small, which is due to the large uncertainties of the measurement. The second region ($0.175 \leq x_\mathrm{F} \leq 0.425$, $0 \leq p_\mathrm{T} \leq 1$ GeV/c) shows that EPOS starts to overestimate the antiproton production for large x_F and the discrepancy grows exponentially. In Fig. 4.6(b) the p_T-integrated spectra for both regions are shown, along with an exponential fit with $\chi^2 = 4.2 \times 10^{-5}$. The reduced χ^2 of a linear fit for both regions is 5.0×10^{-4}. Again, both fits have a very low reduced χ^2, because the uncertainties on the measurement are large. The third region is the upper part of the histogram ($-0.0725 \leq x_\mathrm{F} \leq 0.425$, $1 \leq p_\mathrm{T} \leq 1.6$ GeV/c). The p_T-integrated spectra in Fig. 4.6(c) show a very similar behaviour to the first two regions, with an exponential growth towards higher x_F. The exponential fit has a $\chi^2 = 5.7 \times 10^{-3}$ while for a linear fit $\chi^2 = 0.24$.

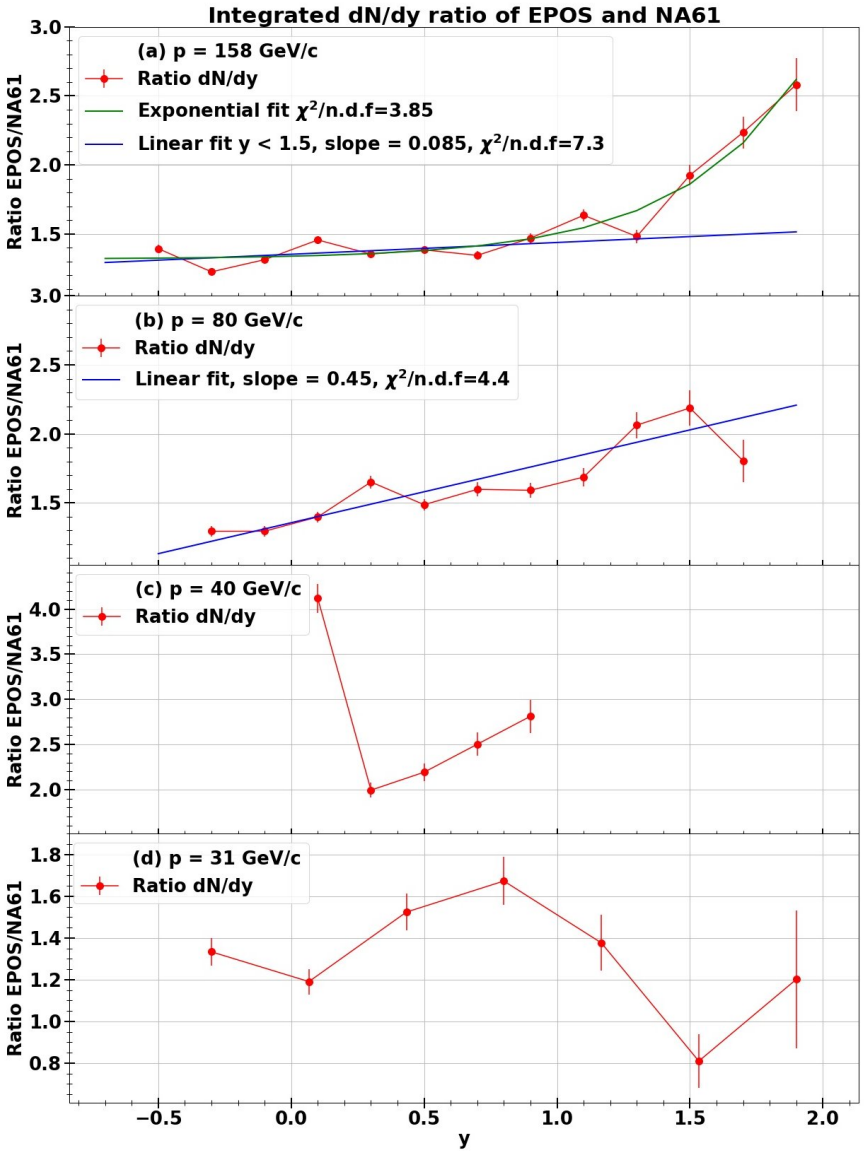

Figure 4.4 Ratios between the p_T-integrated yields dN/dy of EPOS and NA61. Additionally a linear fit for -0.3<y<1.7 and an exponential fit over the whole rapidity range is shown for the momenta considered in **(a)** and **(b)**. The fits have a reduced χ^2 of 7.3 and 3.85 respectively.

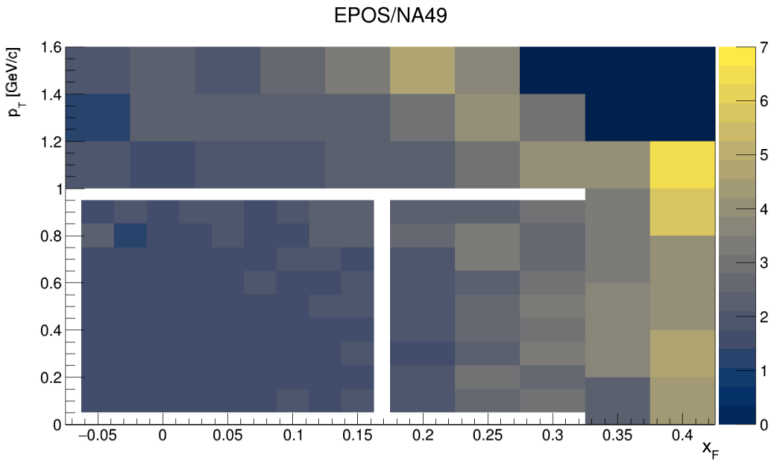

Figure 4.5 Ratio of the prediction from EPOS and the invariant cross section for inclusive antiproton production measured by NA49.

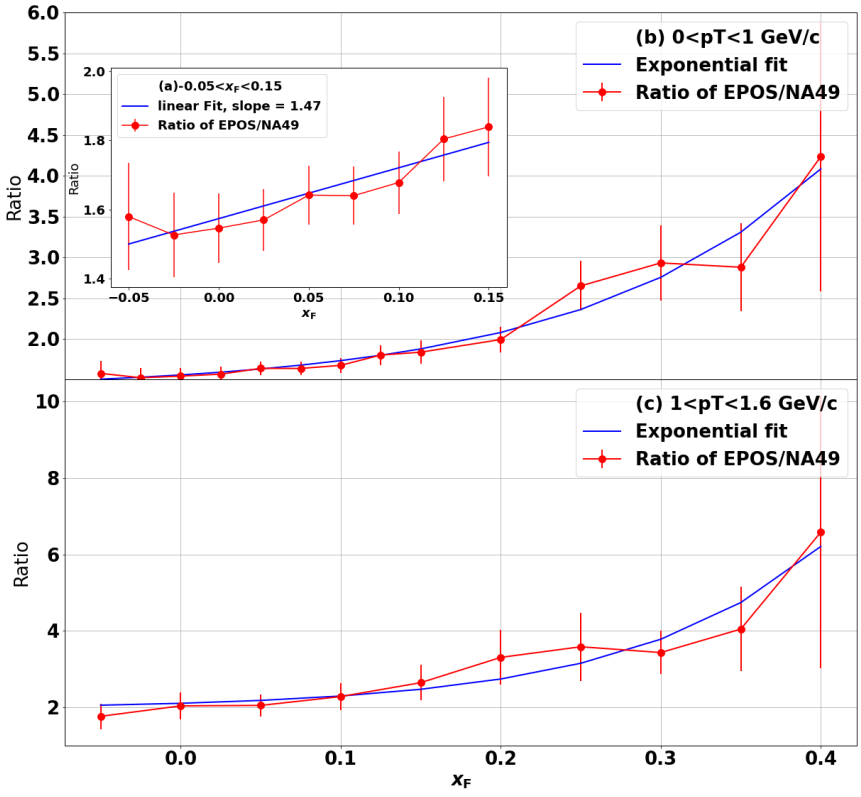

Figure 4.6 Ratio between the integrated $d\sigma/dx_F$ inclusive antiprotons production cross sections of EPOS and NA49. **(a)** shows the central region (x_F=[-0.05,0.15], p_T=[0,1]) and is fitted with a first order polynomial with slope 1.47 $\pm$ 0.25 and $\chi^2 = 2.5 \times 10^{-5}$. **(b)** Shows the full x_F region with p_T=[0,1] and includes an exponential fit with $\chi^2 = 4.2 \times 10^{-5}$. **(c)** shows the upper region for 1<p_T<1.6 in full $x_F$as well as an exponential fit.

4.1.3 BRAHMS

The BRAHMS experiment [48] is located at the Relativistic Heavy Ion Collider (RHIC) at Brookhaven National Laboratory. BRAHMS is dedicated to the measurements in the forward rapidity region. The invariant inclusive antiproton production cross sections as a function of p_{T} are shown in Fig. 4.7a and Fig. 4.7b for the rapidity ranges of $2.9 \leq y \leq 3.0$ and $3.25 \leq y \leq 3.35$, respectively. The rapidity is expressed in the center-of-mass frame. At lower rapidity (Fig. 4.7a), EPOS overestimates on average the production of antiprotons by a factor of 1.54 from p_{T}=[0.8,1.8] GeV/c. There appears to be a hard transition in EPOS around $p_{\mathrm{T}} = 2$ GeV/c, where the shape of the spectrum changes slope and becomes harder than the spectra measured by BRAHMS. The reason for this sudden change is not clear, but for p_{T}>2 GeV/c the average ratio increases to 6.28. At larger rapidity (Fig. 4.7b), EPOS overestimates the production cross section on average by a factor of 3.89. For p_{T} >= 2.8 GeV/c, the low number of candidates does not allow for a meaningful interpretation.
In both cases the shapes of the spectra are not comparable with the data. Interestingly, while the EPOS results are corrected for the contribution from weak decay feed-down, it is unclear whether the measurements carried out by BRAHMS are corrected for this effect [53]. Taking weak decays into account would decrease the production cross section measured by BRAHMS by a factor of roughly 33% at this energy [54]. Including antiprotons from weak decays would not change the overall shape of the spectrum. This is shown in Sec. 4.3.

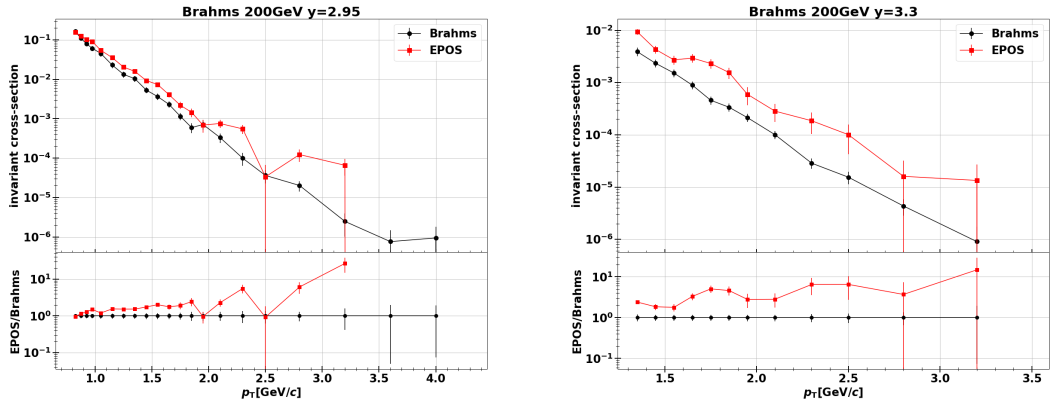

(a) Comparison of BRAHMS data to EPOS. y=[2.9,3.0]

(b) Comparison of BRAHMS data to EPOS. y=[3.25,3.35]

Figure 4.7 Comparison of the invariant inclusive antiproton production cross section measured by BRAHMS [48] and the corresponding EPOS predictions

4.1.4 STAR

In order to gauge the mid-rapidity region at $\sqrt{s} = 200$ GeV, also the measurement of the antiproton production in pp collisions carried out by the STAR collaboration [49] is compared to EPOS predictions. STAR measures invariant yields $1/(2\pi m_{\mathrm{T}})\, \mathrm{d}^2N/(\mathrm{d}m_{\mathrm{T}}\mathrm{d}y)$ as a function of y and $m_{\mathrm{T}} - m_{\mathrm{p}}$, where $m_T = \sqrt{p_T^2 + m_p^2}$ is the transverse mass and $m_p = 0.938$ GeV/c^2 is the proton mass. The measurement is performed at mid-rapidity ($|y| \leq 0.1$). Antiproton

production is also measured in Au–Au collisions (Sec. 4.2.3) by STAR. No correction for weak decays is applied, because the kinematics of antiprotons from $\bar{\Lambda}$ decays are very similar to the kinematics of promptly produced antiprotons. This makes such a correction difficult. Their estimation, derived from measured Λ distributions, gives an effect of about 40%. According to the parameterization in [54], the corrected results would be $(33 \pm 3)\%$ below measured data. Since these numbers agree within 3σ, the estimation made by STAR and the parameterization are in agreement.
In Fig. 4.8, the invariant yields measured by STAR are compared with the predictions obtained with EPOS. The ratio shows a systematic linear drop with transverse mass, from 1.2 to 0.75. The slope parameter is -1.12 ± 0.07 and the reduced $\chi^2 = 4.8$. Even though it is at the exact same energy as BRAHMS, the STAR measurement is reproduced much better by EPOS. This could mean that EPOS is not able to reproduce antiproton production outside the mid-rapidity region(e.g. large y or x_F). This effect could also be observed when comparing EPOS to the results by NA61 (Fig. 4.4) and NA49 (Fig. 4.5), even if less accentuated.

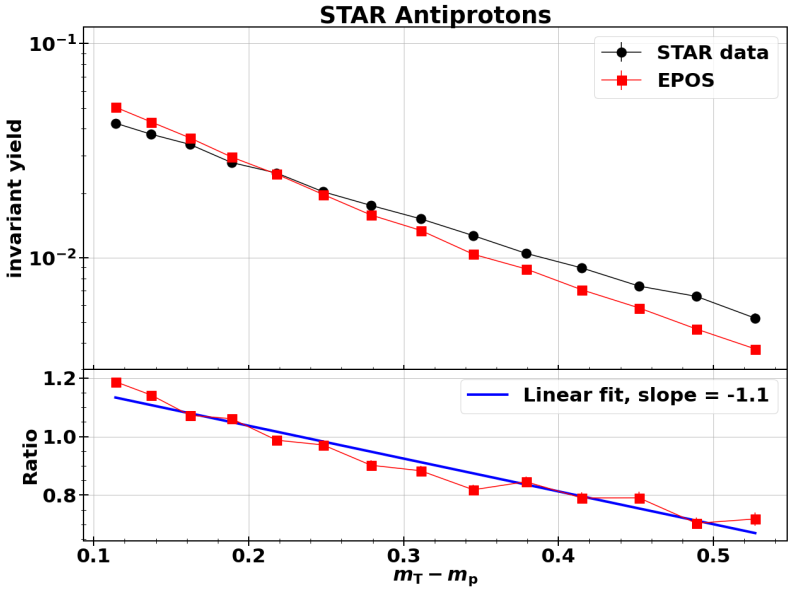

Figure 4.8 Comparison of the data measured by STAR in p–p and the corresponding EPOS simulation

4.2 Other colliding systems

Considering p–A and A–A collisions makes it possible to study the dependence of antiproton production on the system size. A–A collisions are particularly important, because very precise measurements for antideuteron production exist. p–A collisions on the other hand are important for cosmic-ray studies, because 10% of hadrons in the interstellar medium are Helium nuclei and 1% even heavier nuclei and atoms. About 36% of antiprotons in cosmic rays are produced in collisions with He, such as p–He, He–p and He–He, while collisions including heavier nuclei produce an additional 10% [51].

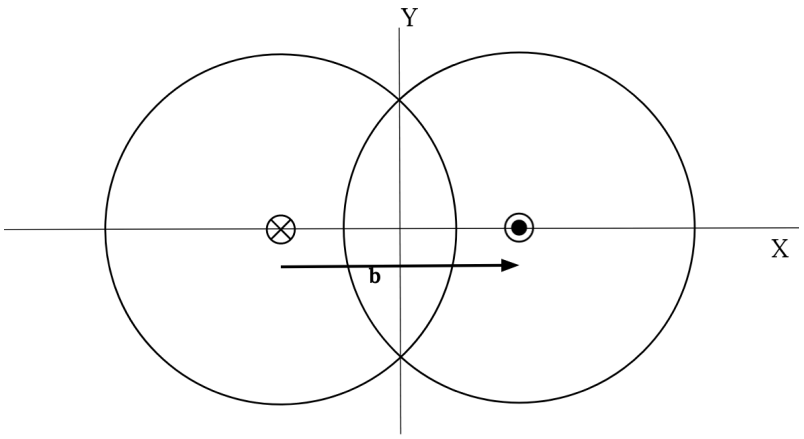

Figure 4.9 Definition of the impact parameter b as the distance between the centers of the colliding nuclei in the plane perpendicular to their direction of movement. The symbols in the center indicate their movement into (out of) the plane as $\otimes$ ($\odot$)

Measurements for heavy-ion collisions are often categorized according to the centrality of the collision. The centrality of a collision is defined by its impact parameter b. In Fig. 4.9, the geometric definition of the impact parameter can be seen. It is the distance between the centers of the colliding nuclei in the plane perpendicular to their direction of movement. The centrality of a collision is denoted in the percentage of collisions with a lower impact parameter. For example, the 0-10% centrality class denotes the 10% most central collisions. A lower impact parameter results in a more central collision and a lower centrality percentile.

4.2.1 NA49 p–C

Besides pp collisions (Sec. 4.1.2), NA49 also measured antiproton production in p–C collisions [46]. In particular, they measured the invariant inclusive production cross section for antiproton $E\frac{\mathrm{d}^3\sigma}{\mathrm{d}p^3}$ as a function of x_F and p_T. The general setup of the experiment is the same as the one used for pp collisions, but a graphite target is used instead of a hydrogen one. The collision energy is still $\sqrt{s_\mathrm{NN}} = 17.3$ GeV in the nucleon-nucleon rest frame.
Fig. 4.10a and 4.10b show the invariant cross section measured by NA49 and the corresponding predictions from EPOS. One can see that the NA49 data show an asymmetric distribution along x_F. The cross section for negative x_F is higher than for positive x_F. Contrarily, the EPOS results are perfectly symmetric in x_F. This can be explained by the absorption of antiprotons inside the carbon nucleus in which they are created and it seems that EPOS does not contain such a feature in its simulation. The shape of the spectra is very different and their ratio varies between 1 at the lowest x_F (x_F=-0.2) up to a maximum of 2.5 at the highest x_F (x_F=0.3). The results for negative x_F also show that EPOS is able to predict the production quite well in the region where no absorption is present. For the region $-0.2 \leq x_\mathrm{F} \leq 0$ the average ratio is only 1.17 while in the region $0 \leq x_\mathrm{F} \leq 0.3$ it is 1.55. In Fig. 4.10c, the ratio of the integrated invariant cross section $\mathrm{d}\sigma/\mathrm{d}x_\mathrm{F}$ is shown. It is fitted with an exponential function with a reduced $\chi^2 = 9.0$. It clearly shows the overproduction at positive x_F and its exponential growth.

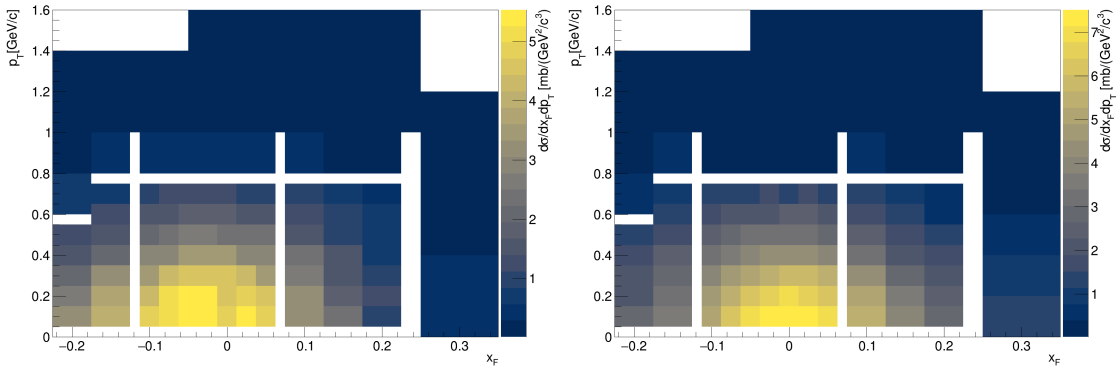

(a) cross section measured by NA49

(b) EPOS prediction of the cross section

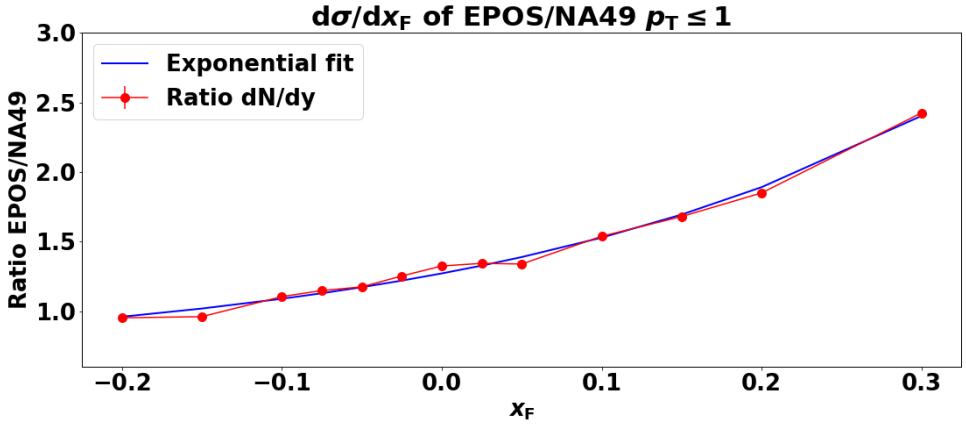

(c) Ratio between the EPOS prediction and NA49 measurement. An exponential fit is shown with $\chi^2 = 9.0$.

Figure 4.10 Results for the invariant inclusive antiproton production cross section for p–C collisions at $\sqrt{s}$=17.3 GeV measured by NA49 **(a)** and the corresponding EPOS prediction **(b)**. A p_T-integrated spectrum with exponential fit is shown in **(c)**. The integration is performed for $0 \leq p_T \leq 1$ GeV/c

4.2.2 LHCb p–He

The LHCb collaboration measured p–He collisions in 2018 [47], obtained by injecting helium gas directly into the LHC beam line and colliding it with a proton beam with a beam energy of 6.5 TeV. The energy of the collision in the Center of Mass (CoM) frame is $\sqrt{s_{\mathrm{NN}}} = 110.5$ GeV. This experiment was the first of its kind and it had a great impact on interpreting recent results from cosmic ray antiproton measurements. Thanks to its capabilities in reconstructing particles at far forward rapidities ($2 < \eta < 5$)[1], the LHCb experiment was able to measure antiprotons with a momentum from 12 to 110 GeV/c and a transverse momentum from 0.4 to 4. GeV/c. LHCb has measured the antiproton production cross sections $\mathrm{d}^2\sigma/\mathrm{d}p\mathrm{d}p_T$ as a function of p and p_T. In Fig. 4.11, the ratio between EPOS predictions and the measured LHCb data is shown and in App A.3 the measurement results from LHCb and the EPOS prediction can be seen. While EPOS decently reproduces the data, with an average ratio to the real measurements of 1.31, at low total momentum and at high p_T it starts to produce a factor of 2 more

[1] -2.8<y^*<0.2 in the nucleon nucleon frame

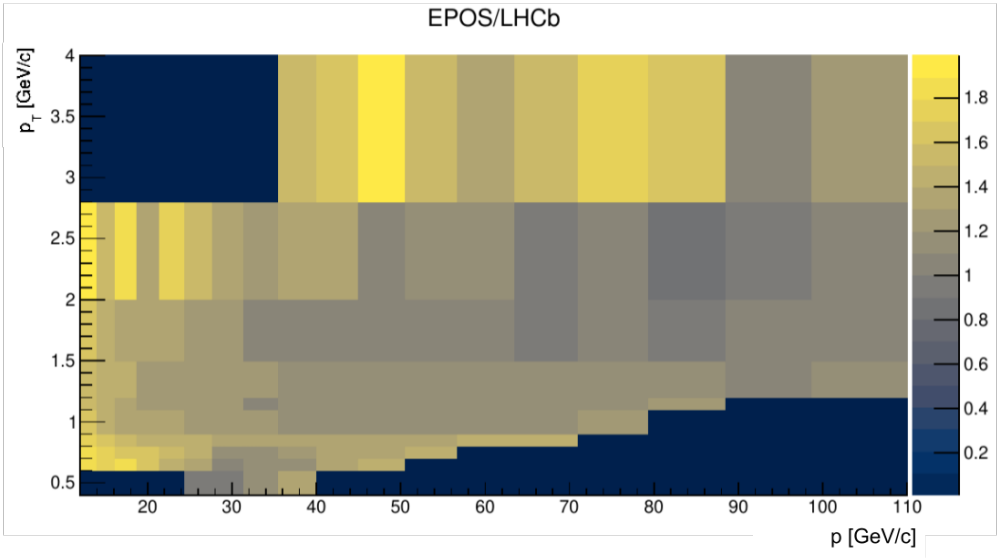

Figure 4.11 Ratio between the EPOS prediction and the measured antiproton production cross section ($d\sigma^2/dpdp_T$) by LHCb.

antiprotons with respect to the LHCb measurement. Since the production of antiprotons by EPOS is consistently higher than the measurement at large p_T, it is unlikely a problem of low number of candidates, but a systematic effect with EPOS.

4.2.3 STAR Au–Au

Lastly EPOS predictions have been compared to measurements carried out in heavy-ion collisions, in particular Au–Au collisions at $\sqrt{s_{NN}}$=200 GeV measured by the STAR collaboration [49] in 2004[2]. The measurement has been carried out in 9 centrality classes (0-5%, 5-10%, 10-20%, 20-30%, 30-40%, 40-50%, 50-60%, 60-70%, 70-80%) at mid rapidity ($|y| \leq 0.1$) as a function of $m_T - m_p$. Similar to Sec. 4.1.4, no corrections for weak decays have been applied. For this thesis, the main interest in this dataset is to be used as a correction for coalescence studies (5.2). The focus is on the 0-5% and 5-10% centrality classes. These centralities correspond to the most central data published for antideuterons in Au–Au collisions by STAR in 2019 [55].
Before comparing the EPOS predictions with the STAR measurement, it needs to be clear that the centralities and impact parameters coincide between STAR and EPOS. In 2009 STAR published an overview of the impact parameter ranges for each centrality in Au–Au collisions at $\sqrt{s_{NN}} = 200$ GeV [56]. Their findings and the corresponding EPOS results can be found in Fig. 4.12. In this case we have a perfect agreement between EPOS and and the measurement by STAR.

[2]Their data can be found in: https://drupal.star.bnl.gov/STAR/files/starpublications/31/data.html

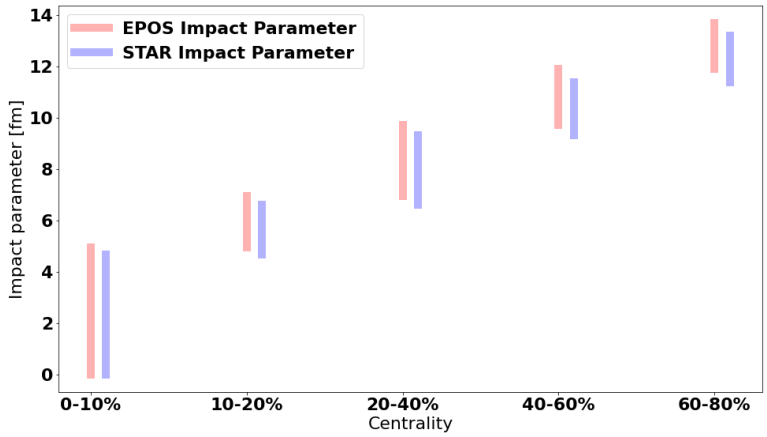

Figure 4.12 The impact parameter range for each centrality class published by STAR [56](blue) and in EPOS (red).

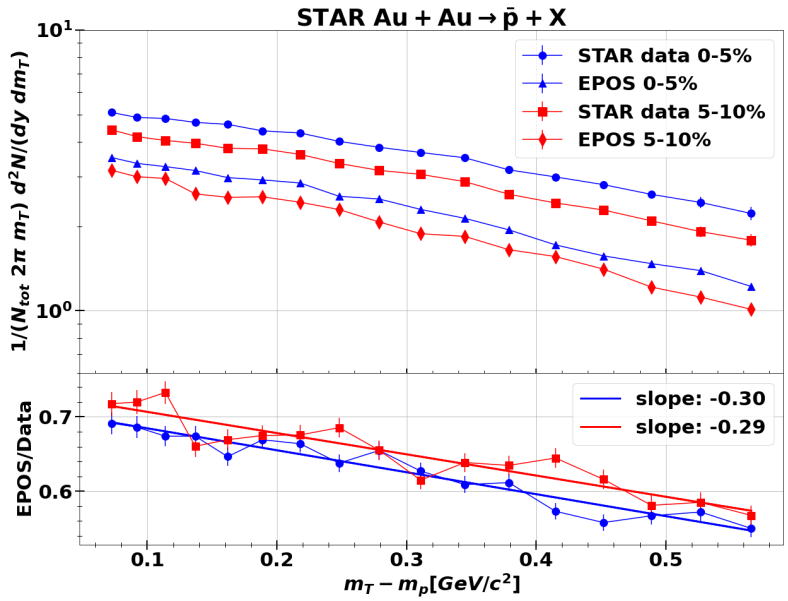

Figure 4.13 STAR Au–Au 200 GeV data compared to EPOS.

In Fig. 4.13, a comparison between STAR's measured results and EPOS predictions are shown. EPOS prediction of antiprotons falls below the measurement by a factor of 1.4 (1.8) at low (high) $m_{\mathrm{T}} - m_{\mathrm{p}}$. The ratio drops off perfectly linear for both centralities. The slope parameter for 0-5% is -0.30 ± 0.02 with reduced $\chi^2 = 1.3$ and for 5-10% it is -0.29 ± 0.03 with reduced $\chi^2 = 2.0$. This shows that they are perfectly parallel within errors, but the more central data is shifted down by around 3%. This is exactly the same behaviour of linear drop-off towards high $m_{\mathrm{T}} - m_{\mathrm{p}}$ observed for pp collisions (Sec. 4.1.4), where the slope was much steeper ($-1.12 \pm$

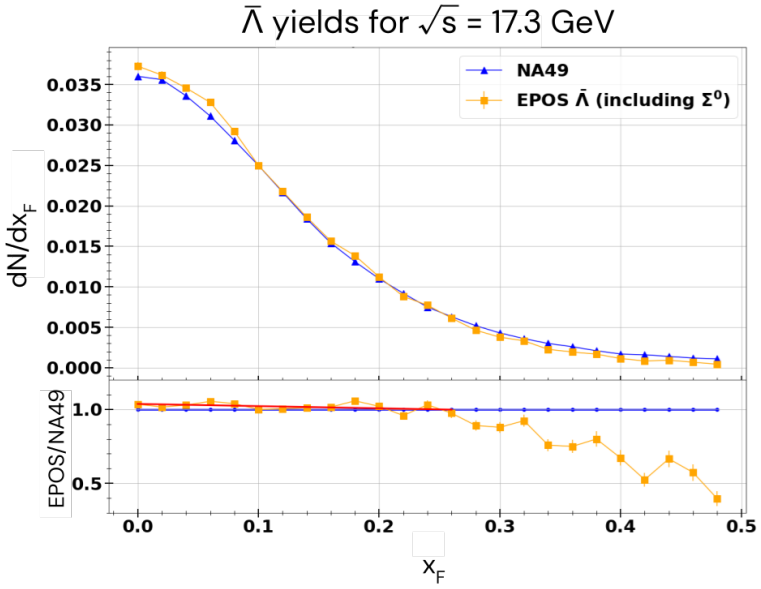

Figure 4.14 $\bar{\Lambda}$ spectra measured by NA49 for 17.3 GeV compared to the corresponding EPOS prediction.

0.07).

4.3 Antiprotons from hyperon decays

As mentioned in Sec. 4.1.3, antiprotons do not only come from prompt production in the collision, but also from long lived resonances like hyperon decays. Hyperons are baryons which are composed of at least one strange quark. Examples of hyperons are the Λ (=uds, I=0) and the Σ (Σ^+=uus, Σ^0=uds, Σ^-=uus, I=1) baryons. Two of these ($\overline{\Lambda}$ and $\overline{\Sigma}^+$) decay directly into antiprotons, with a branching ratio of 64% and 52%, respectively, while the $\overline{\Sigma}^0$ decays into $\overline{\Lambda}$, with a 100% branching ratio.[3] Since the lifetime of these resonances[4] is in the order of 10^{-10}s, they can travel several centimeters before decaying. This means that antiprotons from hyperon decays can often be separated from promptly produced ones, by reconstructing their production vertex. Indeed, many experiments correct their antiproton yields for such feed-down from hyperons. Since for cosmic-ray studies the origin of the antiprotons is not of interest, the contribution of feed-down must be assessed. In Fig. 4.14, the antilambda yields measured by NA49 [57] in pp collisions at $\sqrt{s} = 17.3$ GeV and the corresponding EPOS prediction can be seen. EPOS shows that, when including $\overline{\Lambda}$ from $\overline{\Sigma}^0$ decays, EPOS reproduces the experimental results perfectly up to x_F=0.25. For higher x_F EPOS underestimates the yields. It is fit with a first order polynomial with slope parameter -0.14 ± 0.08 and y-intercept 1.03 ± 0.013 up to x_F=0.25 (χ^2/n.d.f=1.26). The dataset from NA49 has no uncertainty estimation, so it is hard to gauge if this is a problem in NA49 due to a low number of candidates or a systematic

[3] The branching ratio describes the probability of a particle to decay in a specific decay channel. A 64% branching ratio means that the $\bar{\Lambda}$ decays into antiprotons with a 64% probability.

[4] 10^{-20}s for the $\overline{\Sigma}^0$, but it decays into the $\overline{\Lambda}$.

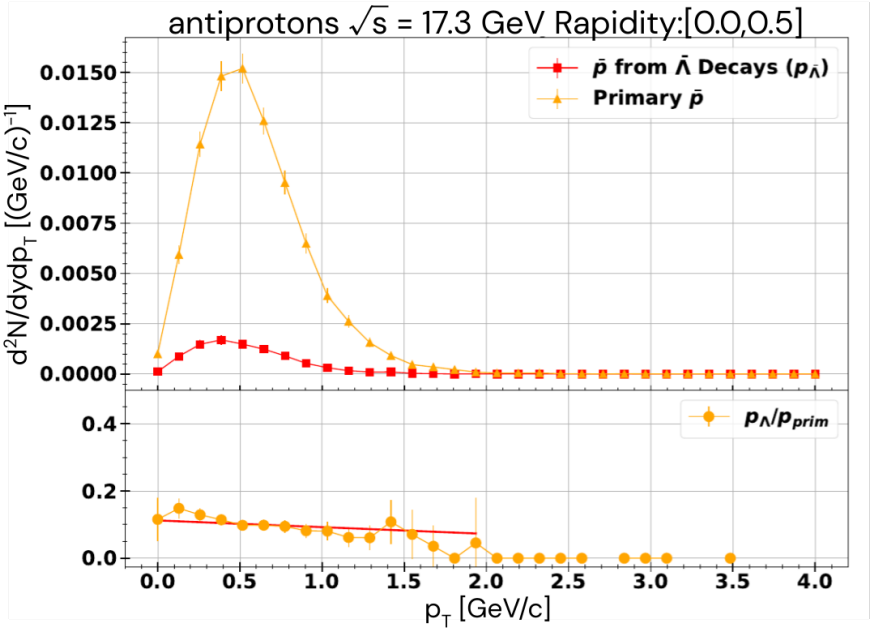

Figure 4.15 EPOS prediction for the primary antiproton spectra and antiproton spectra from hyperon decays for pp collisions at 17.3 GeV at mid-rapidity (0-0.5).

problem in EPOS. In Fig. 4.15 a comparison of the EPOS prediction for promptly produced antiprotons and antiprotons from antihyperon decays is shown. Additionally, the ratio of prompt and feed-down antiprotons is fitted with a first-order polynomial, with y-intercept 0.112 ± 0.009 and slope parameter 0.02 ± 0.013 (χ^2(n.d.f = 0.411). It shows that the spectral shapes agree within 2σ and the feed-down contribution from antihyperons is(11.2 ± 0.9)% at this energy. This means that for cosmic ray studies the spectra from prompt production can simply be scaled up to account for feed-down from hyperons. For coalescence, the antinucleons stemming from hyperon decay do not play a significant role, since they are produced too far from the collision vertex.

4.4 Summary of antiproton data

In Tab. 4.2 EPOS performance is summarized. In general, one can see that the predictions from EPOS need to be corrected in order to properly reproduce the measurements. In the following, the adopted correction scheme is described.

4.5 Correction scheme

The correction is applied on an event-by-event basis. This means that every event or particle is given a unique weight according to a previously determined correction factor. How this correction factor is obtained, is described in the following.
A very simple form of correction is done by comparing a prediction and to measured data. The ratio between the prediction and the measured data is applied as a correction factor to

Experiment	System	Energy [GeV]	EPOS Performance
NA61	pp	7.7, 8.8, 12.3, 17.3	linear growth of overproduction towards high y
NA49	pp	17.3	exponential overproduction towards high x_F
BRAHMS	pp	200	Good shape, but overproduction
STAR	pp	200	Good cross section, but wrong shape
NA49	p–C	17.3	Wrong shape, probably due to absorption
LHCb	p–He	110.5	Overproduction and wrong shape
STAR	Au–Au	200	Underproduction and wrong shape

Table 4.2 Short overview of the experiments discussed in this chapter and EPOS performance when reproducing them

the results of the prediction. This idea can be simply expressed by

$$\underbrace{\left(\frac{f_{\text{Prediction}}}{f_{\text{Data}}}\right)^{-1}}_{\text{Correction Factor}} \cdot f_{\text{Prediction}} = f_{\text{Data}} \tag{4.1}$$

Since data from measurements are generally binned (e.g. p_T, x_F), this simple approach would be a *bin-by-bin* correction. To further generalize this scheme to an *event-by-event* correction one needs a smooth description of the prediction and of the measurement. In this case, smooth means that every point in phase-space gets assigned a unique value instead of grouping a range of values in a bin. In this way also the correction is unique for every point in phase-space and the correction can be applied to each event/particle separately. Such a smooth description can be obtained in different ways, for example via a fit or a spline interpolation[5].
The advantage of fitting is that one can use it to extrapolate beyond the phase-space provided by an experiment, but it requires prior knowledge on the functional form of the measured distribution. In the case of antiprotons, multiple parameterizations have been developed for such tasks [54, 33]. Generally, performing these fits is very laborious and is left to future studies.
Splines are a tool to interpolate data points without any prior knowledge on the functional form of the investigated distribution. One disadvantage of spline interpolation is that they do not allow for extrapolation beyond the phase-space provided by the measurement. Additionally, a spline is constrained to always pass through the central value of each data point touch of the dataset, and is thus not considering the measurement uncertainties.[6]
In this thesis, a spline based correction scheme is used. In particular, the PYTHON library SCIPY.INTERPOLATE, more specifically its RBF[7] function, is employed. RBF stands for *Radial basis function*, which is a function whose value only depends on the distance from the origin. Popular prototypes for RBFs are multiquadric $\left(\phi(x) = \sqrt{1+||x||_2^2}\right)$ or Gaussian $\left(\phi(x) = \exp(-||x||_2^2)\right)$ functions, where $||\cdot||_2$ is the euclidean norm. The final interpolation between n

[5] one can also use triangulation schemes, but these generally yield a non-smooth and thus non-physical description and deliver generally worse results.

[6] This can be mitigated by smoothing and is discussed at a later point

[7] Documentation can be found at: https://docs.scipy.org/doc/scipy/reference/generated/scipy.interpolate.Rbf.html

data-points is then made by linear combinations

$$u(x) = \sum_{k=1}^{n} \alpha_k \phi(||x - y_k||_2) \tag{4.2}$$

of spatially translated functions $\phi(||x-y_k||_2)$ of a single radial basis function prototype, where y_k are the positions of the data-points. Interpolation with RBFs is a so called "meshless" interpolation, which means that the positions of data-points do not have to lie on a regular grid for the interpolation to work [58]. This is useful when interpolating data with irregular binning, like for example NA49 measurements (see Sec. 4.1.2).
Since RBFs are defined solely by the distance from their origin, this scheme can be extended to an arbitrary number of dimensions. This property is useful for interpolating between different experiments, because many experimental results lie on a 2D grid (e.g. $p_T$vs x_F). To interpolate between different $\sqrt{s}$, one needs at least a 3D interpolation. However, for this thesis only proof of concept work was done, so for this work energy interpolation has not been carried out and it is left for future studies.
Another feature of SCIPY.INTERPOLATE.RBF is the capability to smooth the spline. This allows the spline to deviate from the central point, mimicking the effect of uncertainties. This is useful for interpolating experimental results, since measured data always have an uncertainty, which makes it deviate from the underlying functional form. In Fig. 4.16, the antiproton production cross section measured by NA61 (Sec. 4.1.1) for $p_T = 0.35 \pm 0.05$ GeV is shown alongside 4 different spline interpolations, obtained with multiquadric RBFs and by varying the smoothing parameter, which is a positive floating point number given to the algorithm. The relation between the magnitude of the parameter and the effect is not trivial and goes beyond the scope of this work. However, it is possible to see how in each case under study the spline interpolation provides a smooth function of rapidity and that the main effect of the smoothing procedure concerns the point at y = 0.3. To obtain the goodness of a spline to a dataset is not as trivial as with fits, where a χ^2 can be computed and minimized. Indeed the goodness of a spline cannot be evaluated via a χ^2 minimization, because for a non-smoothed spline the χ^2 is null by definition. As discussed above, smoothing is a desirable feature in a spline. For this reason, the smoothing parameter that reproduces best the experimental measurements, mitigating the statistical fluctuations, is arbitrarily chosen. In Fig. 4.17 a schematic overview of the correction scheme is shown. Fig. 4.17a shows the ratio between the EPOS prediction and the experimental results before applying the correction scheme. Fig. 4.17b shows the spline interpolation of the EPOS prediction and the measurement. The ratio between these two splines is used as an event-by-event correction. This correction is now a smooth function of the kinematic variables used by the experiment. To get a corrected result (seen in Fig. 4.17c), the EPOS output is reanalyzed. For every particle of interest (in our case every antiproton), its position in phase-space is determined. The value of the correction function at this point is taken as a weight for each particle when reconstructing the measurement. However, it is important to notice that if a fluctuation is present in the original dataset it will also be present in the corresponding spline, hence every time that the correction is applied. For example, the spline obtained from NA61 data is affected by the fluctuation at y=0.3. In order to test this effect, the correction evaluated from NA61 is applied to NA49 data. These two experiments are chosen because they are characterized by the same collision energy. When using two different datasets, the scheme in Fig. 4.17 becomes only slightly more complex. First, a correction function is obtained of the first experiment, in this case NA61. It is possible that

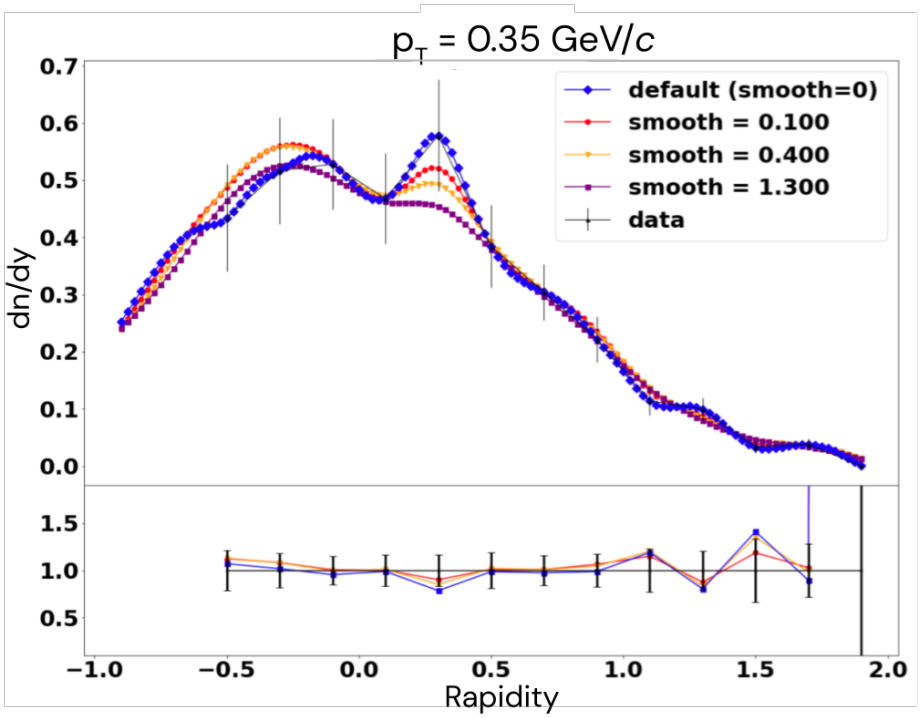

Figure 4.16 Invariant inclusive antiproton production cross section as a function of rapidity measured by NA61 at $p_T = 0.35 \pm 0.05$ GeV/c. Additionally interpolations using multiquadric Radial Basis Functions with smoothing parameters for 0, 0.1, 0.4 and 1.3 are shown.

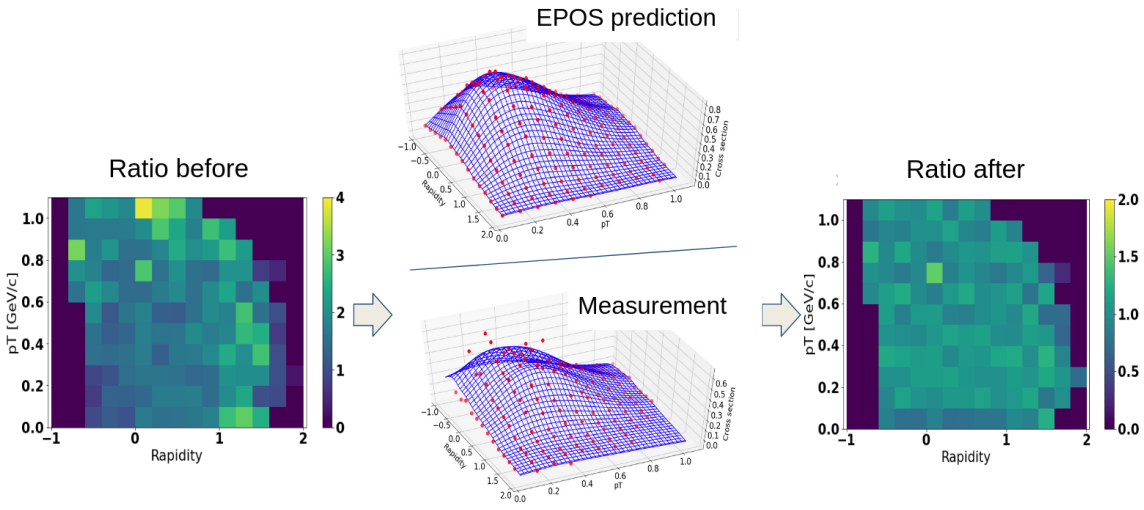

(a) Ratio between a measurement and the corresponding EPOS prediction

(b) Spline interpolation of the measurement and EPOS. The ratio of the splines of EPOS and of the measurement is used as a correction

(c) Ratio between the measurement and the corrected EPOS prediction

Figure 4.17 Schematic overview of the correction scheme employed in this thesis using spline interpolation.

two different sets of kinematic variables are used in the two experiments. If they are the same, the correction obtained from the first experiment can be directly applied to the second one. Otherwise, first it is necessary to evaluate the correction using the kinematic variable of the first experiment and convert them to those used in the second one.
The advantage of doing it in this way is that the correction now gets independent of possible outliers in the first experiment, since it is highly unlikely that the second experiment has the same fluctuations. This means, that a spline following a fluctuation, like the one shown above, would give larger deviation compared to a spline where such outliers have been smoothed out. Also it is now possible to gauge to goodness of the two smoothing parameters using a χ^2 approach, since now the most physically correct shape of the spline yields the best results.

4.6 Corrected results

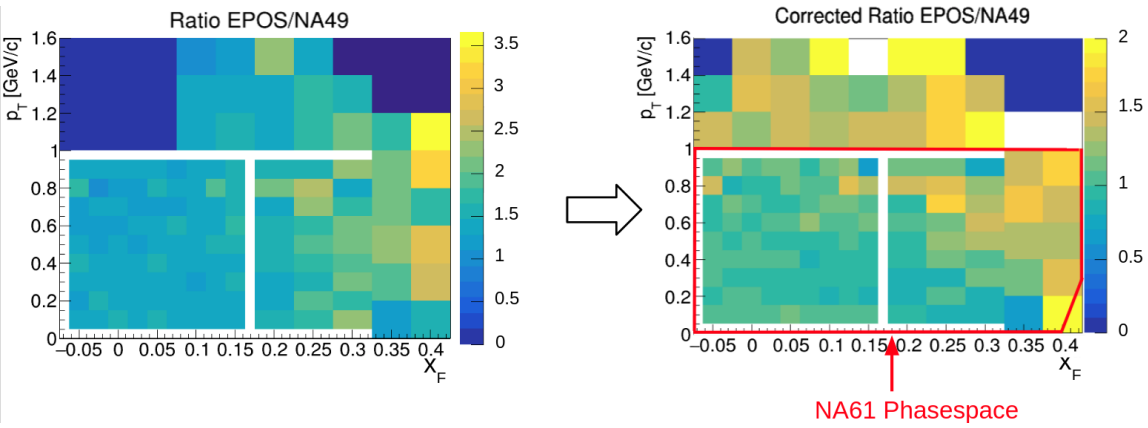

(a) Ratio of the EPOS prediction of the invariant antiproton production cross section with the NA49 measurement presented in Sec. 4.1.2

(b) Ratio of the corrected EPOS prediction of the invariant antiproton production cross section with the NA49 measurement. The red box shows the overlap in phase-space between NA61 and NA49.

Figure 4.18 Ratio of the EPOS prediction of the invariant antiproton production cross section with the NA49 measurement before **(a)** and after **(b)** the correction using the scheme explained above using the NA61 measurement presented in Sec. 4.1.1

In Fig. 4.18a the ratio of the invariant cross section predicted by EPOS and the measurement by NA49 is shown. In Fig. 4.18b, instead the ratio of the invariant cross section predicted by EPOS after the correction with the above described scheme and the measurement by NA49 is shown. The area circled in red shows the part of the phase-space where NA61 and NA49 overlap, i.e. where the correction scheme can be applied. In the region outside the red box, the correction is extrapolated from the splines. Fir this reason, these points are excluded from this analysis. Also the bottom right bin (x_F=0.4,p_T=0.1 GeV/c) is excluded, because it does not completely lie in the red bod.
Before the correction, the χ^2/d.o.f of the EPOS prediction compared to the NA49 measurement for the area in the red box is χ^2/d.o.f = 74.53, while after the correction it is χ^2/d.o.f = 1.04. This shows a huge improvement in the quality of the prediction made by EPOS.
Fig. 4.19 shows the p_T-integrated ratio between the corrected EPOS prediction and the invariant cross section measured by NA49. The ratio is fitted with a first order polynomial, with a

y-intercept of 1.04 ± 0.03 and a slope of -0.12 ± 0.16, which shows that the adopted correction procedure works really well.

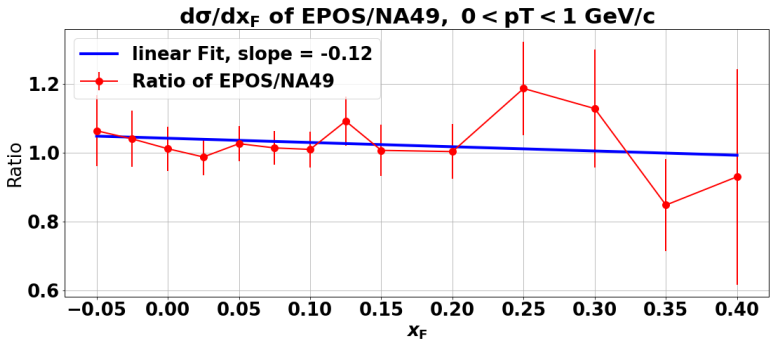

Figure 4.19 Ratio between the corrected integrated inclusive antiproton production cross sections $d\sigma/dx_F$ predicted by EPOS and measured by NA49.

4.7 Summary of spline interpolation

While in Sec. 4.6 the power of the correction method using spline interpolation is discussed, the questions still stands whether splines are the best method when trying to correct event generator output. The answer here is that splines cannot be seen as the solution. They possess no predictive power beyond the phase-space provided to them. Since they struggle with sparse datasets, a large amount of data would be required to span the range $6 \leq \sqrt{s} \leq 200$ GeV, which simply do not exist. While many experiements have been carried out for $\sqrt{s} \leq 17.3$ GeV, the region between 17.3 and 200 GeV has been tested very rarely. The only modern experiment to measure in this region was PHENIX [59] at $\sqrt{s}$=62 GeV. Older experiments, from the 1960s and 70s, at CERN [60, 61, 62] and Fermilab, [63, 64] also exist, but these either have large uncertainties or no estimation of uncertainties was attempted. Additionally, the necessity of an eyeball fit, and thus the impossibility of complete automation of the interpolation process, makes evaluating the quality of a 4D spline (3 kinematic dimensions and one for the value of the cross section) impossible.

Chapter 5

Anti-Deuteron production in EPOS

As discussed in Sec. 1, antideuterons are an interesting probe for indirect dark matter (DM) detection. Following the efforts to correct the antiproton production in EPOS 3 as described in Chapter 4, in the following the results of coalescence in the EPOS event generator are presented. Since EPOS does not have an inherent way to produce light nuclei, an afterburner to the simulation results has been developed, employing the two different approaches to coalescence, the spherical approximation and the coalescence using the Wigner function.

5.1 Available experimental data

Experiment	Reaction	Energies [GeV]	Year	Centrality	Citation
ALICE	pp	7,000, 13,000	2019/20	MB and HM	[65]
ALICE	p+Pb	5,020	2019	5 centrality classes (0-100%)	[66]
STAR	Au–Au	11.5,14.5,19.6, 27,39,62.4,200	2019	5 centrality classes (0-80%)	[55]
Na49	Pb–Pb	17.3	2012	3 centrality classes (0-23.5%)	[67]
Brahms	Au–Au	200	2011	0-20% centrality	[68]
PHENIX	Au–Au	200	2004	0-20% and 20-92%	[69]
STAR	Au–Au	130	2001	Minimum bias	[70]
NA44	Pb–Pb	17.3	2000	0-5% and 5-10%	[71]
AGS	Au–Pt	11.5	2000	Minimum bias	[72]

Table 5.1 Excerpt of existing antideuteron measurements by energy and centralities.

Experimental data for low-energy antideuteron production are scarce. Since the production of multiple antinucleons is suppressed close to the threshold of $6m_{\mathrm{p}}$ a high number of events would be needed to measure enough candidates in order to obtain a statistically significant result. In Tab. 5.1 an excerpt of recent antideuteron measurements is shown. Older measurements, mainly from the 1970s (e.g. [73, 74, 75]), have either very large uncertainties or no

uncertainty estimation was attempted, which makes the comparison to MC predictions difficult. Recent measurements were either carried out with heavy ions such as Au–Au or Pb–Pb or at high energies like the ALICE measurements at the LHC. Since the measurements by STAR and ALICE are the most recent and accurate studies only those were considered in this study. Comparisons of the EPOS predictions to other measurements is planned for future studies. In order to compare the output of EPOS, which does not simulate the creation of light nuclei, to the measurements, an event-by-event coalescence afterburner is used. This afterburner considers each event simulated by EPOS separately and for each antiproton-antineutron pair created it determines whether they coalesce and form an antideuteron. This is either done using the spherical approximation or using the Wigner function approach, as explained in Sec. 2.2.2. Since event generators are known to not perfectly describe nature, some parameters of the generator that are important for coalescence need to be corrected. The coalescence model is sensitive to the spatial distribution of nucleons, because it takes the distance between the created particles into account. It is also sensitive to the momentum distribution of nucleons, since the coalescence probability depends on momentum, either as a step function in the spherical approximation or as a Gaussian (Eq. 2.20) in the Wigner function approach. In addition to this, the coalescence model requires the correct amount of $\bar{\mathrm{p}} - \bar{\mathrm{n}}$ pairs in the same event. In experiments this value is driven by the charged-particle multiplicity. As antiprotons and antineutrons are produced in the same amounts up to an isospin factor, a larger number of charged particles means a higher number of antinucleon pairs. In the following, attempts to correct these parameters, the spatial and momentum distribution as well as the charged-particle multiplicity, in the EPOS simulation are performed for each investigated colliding system and energy.

5.2 STAR Au–Au

The STAR experiment [55][1] measured the antideuteron production in Au–Au collisions at a center of mass energy per nucleon-nucleon pair of $\sqrt{s_{\mathrm{NN}}} = 11.5$, 14.5, 19.6, 27, 39, 62.4 and 200 GeV. They measured differential yields $1/(N_{\mathrm{evt}} 2\pi p_{\mathrm{T}}) \mathrm{d}^2N/(\mathrm{d}p_{\mathrm{T}}\mathrm{d}y)$ as a function of p_{T} in a rapidity window of |y|<0.3. Their results are divided into 5 centrality classes: 0-10%, 10-20%, 20-40%, 40-60% and 60-80%. As a first step for this analysis only the highest-energy (200 GeV) and most central (0-10%) collision is considered, as this measurement has the largest number of candidates and thus the best precision. Investigating the other energies and centrality classes is left for future studies. The comparison of centralitiy classes in EPOS and the measured ones has already been discussed in Sec. 4.2.3. It is shown that centrality is reproduced almost perfectly in EPOS (Fig. 4.12). Since centrality and charged-particle multiplicity are closely related, no further correction to the multiplicity distribution was performed.

Fig. 5.1 shows a measurement of the pion emission source radii by the STAR collaboration. It is compared to the corresponding size in EPOS, also obtained using the pion emission source. It shows that for central collisions EPOS reproduces the source size within 5%, while for peripheral collisions this discrepancy grows. Since for this analysis only the most central collisions are of interest, no further corrections to the emission source of EPOS are performed. For the correction of the momentum distribution, the results from Sec. 4.2.3 are used and the correction is applied to antiprotons and antineutrons equally, meaning that a perfect isospin

[1] Their data can be found at https://drupal.star.bnl.gov/STAR/files/starpublications/302/data.html

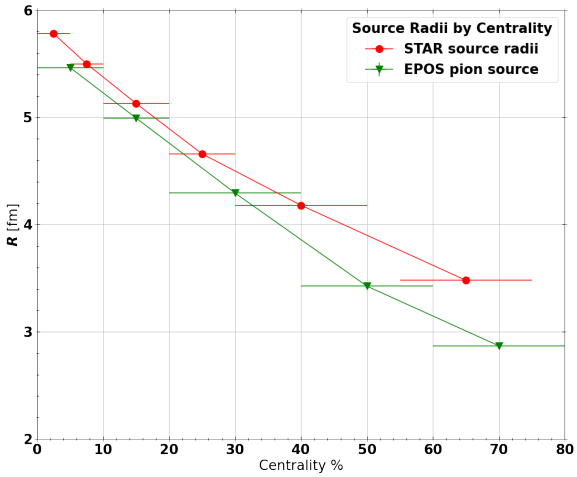

Figure 5.1 Comparison of the Au–Au emission source in STAR at $\sqrt{s} = 200$ GeV to the corresponding pion emission source in EPOS. Data taken from [76]

symmetry is assumed in momentum space. Fig. 5.2 shows the antideuteron yields obtained from a coalescence afterburner using spherical approximation and the Wigner function approach. The results for the spherical approximation are shown for 3 different values of p_0, 200, 250 and 300 MeV/c as well as bands indicating the results for r_0 from 2-4 fm for each coalescence momentum. The lower edge corresponds to an r_0 value of 2 fm, the upper edge to 4 fm. The errorbars shown are the statistical uncertainties for each r_0 value. It is very clear that for multiple combinations of p_0 and r_0 the exact same result can be obtained. This can be seen in panel (a) and (b) of Fig. 5.3. In panel (a) the ratios between the predictions for r_0 = 4 fm and 2 fm for every coalescence momentum are shown along with linear fits. The fits have slopes of -1.18 ± 1.10 (200 MeV/c, χ^2/n.d.f = 3.2), -1.07 ± 0.85 (250 MeV/c, χ^2/n.d.f = 0.94) and -0.061 ± 0.289 (300 MeV/c, χ^2/n.d.f = 1.02), so they are all compatible with 0 within 2σ. In panel (b) the ratios between $p_0 = 250$ MeV/c and 200 MeV/c for $r_0 = 2$ fm and 4 fm are shown, again with linear fits. The fits have slopes of -0.14 ± 0.33(2 fm, χ^2/n.d.f = 0.12) and 0.13 ± 0.65(4 fm, χ^2/n.d.f = 0.21), so both are, again, compatible with 0 within 1σ. This flatness in the ratios shows that changing the values for p_0 or r_0 does not change the shape of the spectra, but only their magnitude. This means that e.g. increasing p_0, which increases the yield, can be counteracted by decreasing r_0. From this one has to conclude that p_0 and r_0 are not physical parameters, but merely fit parameters, which incorporate a multitude of other parameters and effects. They need to be determined for each colliding system and energy separately.

In panel (a) of Fig. 5.2, also the result for the coalescence afterburner using the rejection function from the Wigner function approach (Eq. 2.20) is shown. In panel (b), its ratio to STAR data is shown alongside a linear fit with slope parameter -0.068 ± 0.078 and y-intercept 0.68 ± 0.06 (χ^2/n.d.f=0.070). The coalescence approach using the Wigner function perfectly reproduces the shape of the spectrum, but it predicts 32 ± 6% less antideuterons than measured.

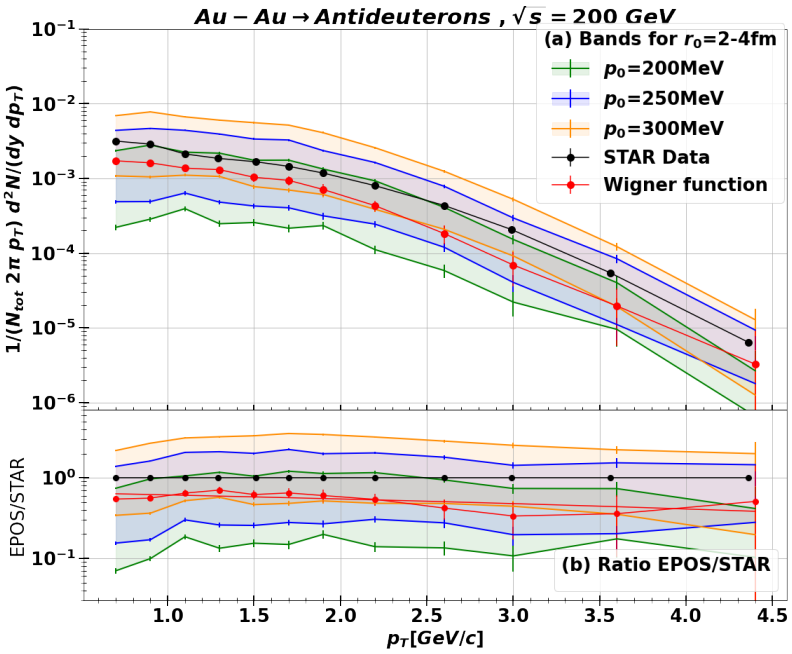

Figure 5.2 **(a)** Antideuterons produced in Au–Au collisions at 200 GeV for 3 different values of p_0 obtained from a spherical approximation coalescence afterburner in EPOS. Bands indicate the yields for r_0 value from 2-4 fm. The lower edge corresponds to an r_0 value of 2 fm, the upper edge to 4 fm. The errorbars shown are the statistical uncertainties for each r_0 value. Additionally the yield obtained from employing the Wigner function approach is shown. **(b)** Ratio between EPOS predictions and STAR results. Bands again indicate r_0 values from 2-4 fm. For the Wigner function approach a linear fit is shown. STAR data are taken from from [55]

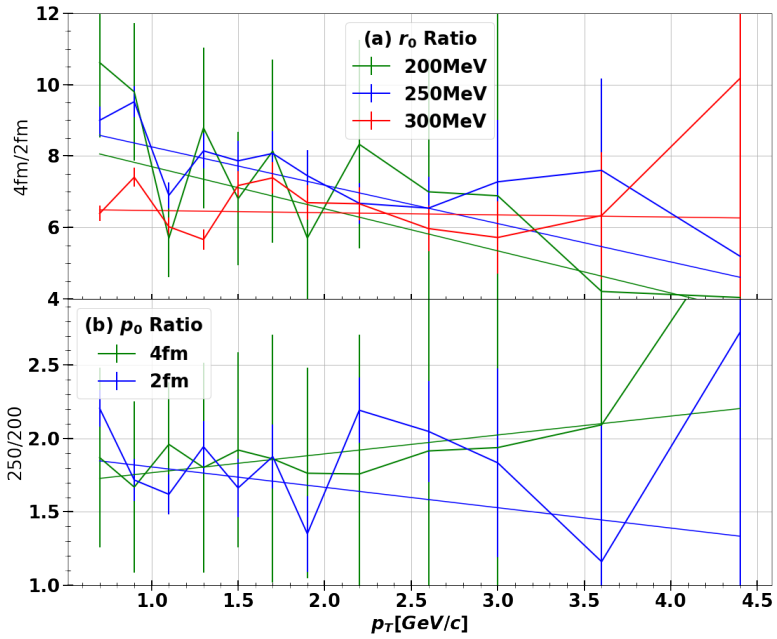

Figure 5.3 **(a)** Ratio between r_0=4 and 2 fm for each p_0 alongside a linear fit. **(b)** Ratio between the results for p_0 = 250 MeV/c and 200 MeV/c for r_0 = 4 and 2 fm and linear fits.

5.3 ALICE pp 13 TeV high multiplicity

The next dataset with which the predictions from EPOS with the coalescence afterburner is compared is a measurement by the ALICE collaboration of antideuteron yields in pp collisions at $\sqrt{s}$ = 13 TeV at mid-rapidity (|y|<0.5) [65]. This measurement only considers the 0-0.01% multiplicity range[2]. This means that EPOS needs to be tuned to reproduce this multiplicity distribution at mid-rapidity. In Fig. 5.4, the multiplicity distribution measured by ALICE at mid-rapidity[3] for this high-multiplicity measurement is shown. Additionally the corresponding EPOS multiplicity obtained via the prescription described in the following can be seen.
In order to reproduce the mid-rapidity multiplicity distribution measured by ALICE, an ALICE-like multiplicity trigger was implemented in the EPOS afterburner. This means that, similar to the implementation in the ALICE experiment, charged particles in the rapidity region covered by the V0 detector (-3.7 < η < -1.7 and 2.8 < η < 5.1, called in the following as V0M multiplicity) are correlated with those in the mid-rapidity region (-0.5 < η < 0.5). This correlation is shown in Fig. 5.5. Then, for each possible minimal V0M multiplicity selection, the resulting mid-rapidity multiplicity distribution is determined. Using a χ^2 test the best matching distribution and its corresponding trigger multiplicity are determined. The best fit is obtained for $N_{\mathrm{ch}}^{\mathrm{V0M}} \geq 127$ ($\chi^2 = 0.00167$).

[2]Multiplicity is very similar to centrality discussed in Sec. 4.2. 0-0.01% means that these are the 0.01% events with the highest charged-particle multiplicities in forward rapidity
[3]Obtained from a private conversation with David Dobrigkeit Chinellato

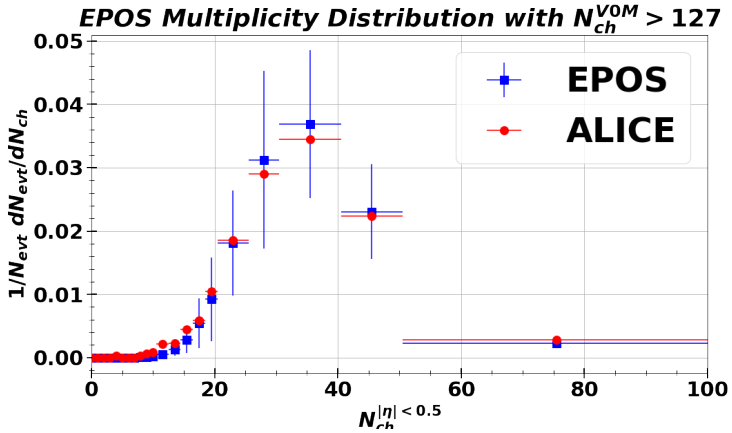

Figure 5.4 Mid-rapidity multiplicity distribution measured by ALICE in 13 TeV high-multiplicity pp collisions. Compared to EPOS results after selecting only event with a V0M multiplicity of >127.

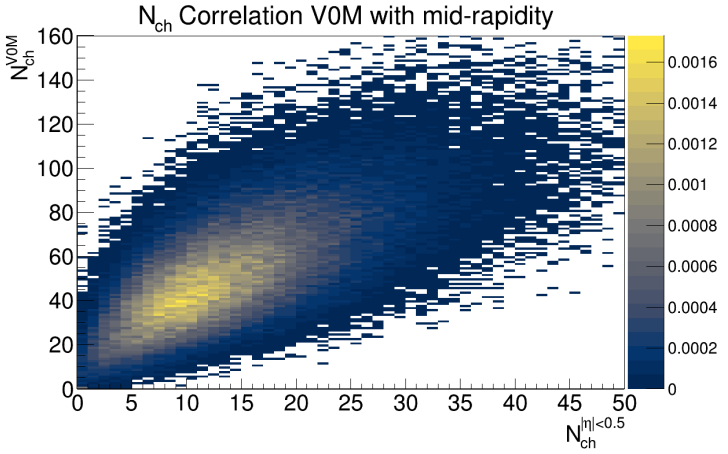

Figure 5.5 Correlation of V0M multiplicity and mid-rapidity multiplicity in EPOS for a pp collision at 13 TeV.

As shown in [30], EPOS 3 does not reproduce the emission source size correctly. For this reason, in this work the measurement of the emission source size carried out by ALICE [30] in the same collision system is used. The measurement is carried out for different particle species and as a function of the transverse mass $m_{\mathrm{T}} = \sqrt{p_{\mathrm{T,p}}^2 + m_{\mathrm{p}}^2}$ and the results are shown in Fig. 5.6. In this case, the effective radius of the source is used, i.e. the radius obtained considering also nucleons coming from the strong decay of resonances, such as Δ^+ and N(1440). The contribution from resonances increases the source size by 5-10% in the case of nucleons. The source is assumed to be Gaussian

$$S_{4\pi}(r) = \frac{4\pi r^2}{(4\pi\sigma^2)^{3/2}} \times \exp\left(-\frac{r^2}{4\sigma^2}\right), \tag{5.1}$$

where sigma is the source size. Operatively, for each proton-neutron pair the average transverse mass is evaluated, hence the average source size is determined. Using Eq. 5.1 as probability distribution, a proton-neutron distance is sampled with the rejection method.

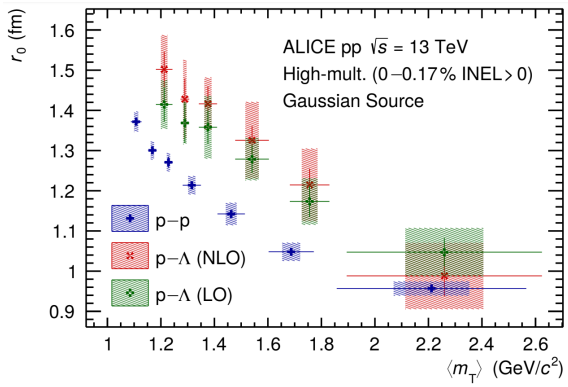

Figure 5.6 Source radius r0 as a function of $\langle m_{\mathrm{T}} \rangle$ for the assumption of a purely Gaussian source. The blue crosses result from fitting the p–p correlation function with the strong Argonne v_{18} potential. The green squared crosses (red diagonal crosses) result from fitting the $p-\Lambda$ correlation functions with the strong χEFT LO (NLO) potential. Statistical (lines) and systematic (boxes) uncertainties are shown separately. Taken from [30].

As last step, the momentum distribution of the nucleons needs to be corrected. For this purpose, the ratio between the p_{T} spectra simulated by EPOS and measured by ALICE is used. The spectra and their ratio are shown in Fig. 5.7. They are p+$\bar{\mathrm{p}}$ spectra, as full matter-antimatter symmetry is assumed at such high collision energies and combining both reduces the statistical uncertainty. The ratio between the ALICE measurement and the EPOS prediction, as described in Sec. 4.6, is used as a correction function.

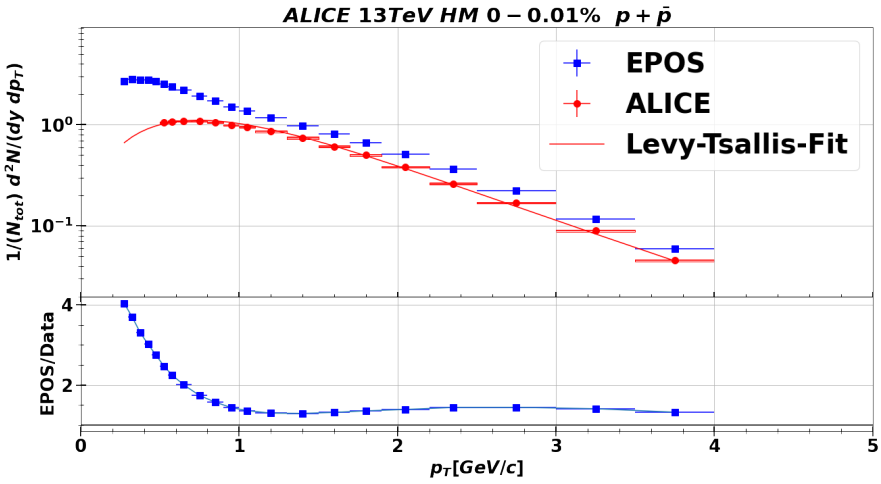

Figure 5.7 p+$\bar{\mathrm{p}}$ yields measured by ALICE in pp collisions at $\sqrt{s}$=13 TeV in the 0-0.01% multiplicity percentile. The EPOS results also contain the multiplicity selection described above.

In Fig. 5.8, the antideuteron production spectra $\frac{1}{N_{\mathrm{HM}}} \frac{\mathrm{d}^2 N}{\mathrm{d}y \mathrm{d}p_{\mathrm{T}}}$ measured by the ALICE collaboration in pp collisions at $\sqrt{s} = 13$ TeV for the 0-0.01% multiplicity class is shown. The experimental data are compared with the predictions from EPOS 3 with a coealescence afterburner based on two approaches: one with a spherical approximation with $p_0 = 100$ MeV/c and no selection on distance, the other based on the Wigner function. The p_0 value is chosen ar-

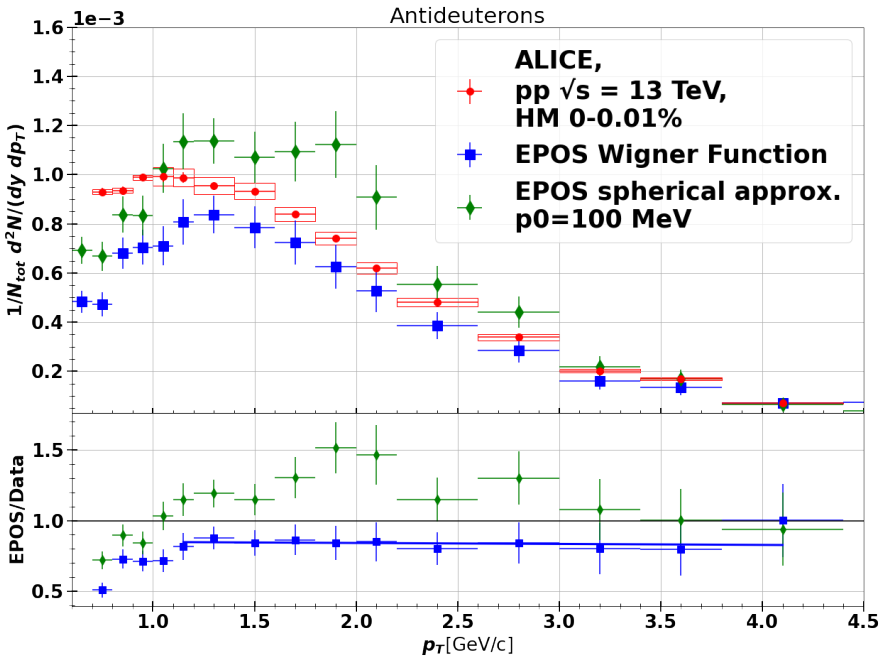

Figure 5.8 p_{T} spectrum of antideuterons in HM pp collisions at $\sqrt{s} = 13$ TeV measured by the ALICE collaboration, compared with the prediction of EPOS with a coalescence afterburner. Green points correspond to the prediction using the spherical approximation, blue points correspond to the prediction using the Wigner function approach. ALICE data taken from [65].

bitrarily to compare the shapes of the spectra. Changing the value of p_0 would only shift the spectra up or down, but not change their shape. There is no selection made on distance, since pp collisions are characterized by a source size smaller than the deuteron size.
The prediction for the spherical approximation completely fails to reproduce the shape of the spectrum. The afterburner using the Wigner function approach reproduces the shape of the measured p_{T} spectra well for $p_{\mathrm{T}} > 1.1$ GeV/c. However, the afterburner underproduces antideuterons by $\sim 14 \pm 12\%$. This range is fitted with a first-order polynomial with a slope parameter of 0.00691 ± 0.0548 and a y-intercept of 0.86 ± 0.12. The EPOS prediction for $p_{\mathrm{T}} < 1.1$ GeV/c falls significantly below the measurement. In this region the antiproton momentum distributions used to correct the antideuteron spectra need to be extrapolated using Lévy-Tsallis functions. This could introduce a systematic bias, which will be part of future investigations.
When comparing the EPOS prediction using the Wigner function coalescence afterburner with the ALICE measurement one can see that the shape of the spectrum from EPOS starts to deviate from the shape of the spectrum measured by ALICE below the peak around $p_{\mathrm{T}} = 1.2\,\mathrm{GeV}/c$. Unfortunately, the spectrum measured by STAR does not cover a low enough p_{T} range to see the results below the peak. This area would be interesting to compare to the afterburner, to see if it also starts to deviate in this colliding system.

Chapter 6

Summary and Outlook

In this thesis, the coalescence model as a mechanism of light nuclei formation is investigated. Two different implementations are used: first, the spherical approximation, which has been commonly used in the last years, and second, the coalescence approach using the deuteron Wigner function, which is a recent development in coalescence studies. Furthermore, corrections to the momentum distribution of nucleons produced by the event generator EPOS 3 are performed, using a correction scheme developed for this thesis. This correction is then used to get precise predictions of antideuteron yields using a coalescence afterburner, which are compared to measurements by STAR and ALICE.

While the spherical approximation reproduces the overall yields for the right choice of the coalescence parameters p_0 and r_0, the shape of the spectra is not correct. It is shown that multiple choices of the parameters p_0 and r_0 in the spherical approximation can lead to the same results. The Wigner function approach, on the other hand, reproduces the shape of the spectra well for intermediate and high p_T, while creating too few antideuterons at low p_T. Comparisons to measurements by ALICE in pp collisions at $\sqrt{s} = 13$ TeV collected with a high-multiplicity trigger show that the Wigner function approach exactly reproduces the shape down to $p_T = 1.2$ GeV/c. Below 1.2 GeV/c EPOS produces significantly less antideuterons compared to measured results. In the higher p_T region EPOS predicts (14 ± 12)% less antideuterons than the measurement. In the case of Au–Au collisions at $\sqrt{s_{NN}} = 200$ GeV, the Wigner function approach produces (32 ± 6)% less antideuterons while precisely reproducing the shape down to $p_T = 0.7$ GeV/c. Measurements of lower p_T are not available for this experiment. These would be interesting to see whether there is a substantial underproduction by the EPOS prediction compared to measurement results.

In future studies the impact of the isospin asymmetry needs to be assessed. While EPOS 3 produces around 40% more antineutrons than antiprotons in pp collisions at 13 TeV, it produces the two types of antinucleons in equal amounts in Au–Au collisions at 200 GeV. Estimations by [54] obtain an inverted relation with the collision energy. They predict perfect isospin symmetry for collisions with energies in the TeV region and $\Delta_{IS} = 0.05 \pm 0.05$ at 200 GeV. Furthermore, the coalescence approach using the Wigner function needs to be tested across a wide range of energies and collision systems, to assess the effect seen at low p_T.

Using the workflow developed in [51], one can implement Monte Carlo predictions for the antideuteron yield in a cosmic ray propagation software such as GALPROP [77]. With the coalescence afterburner presented in this thesis, it is possible to estimate antideuteron production without any free parameters such as the coalescence momentum. This allows to create a

prediction for a large range of collision energies without requiring experimental data and to improve the calculations for the secondary and tertiary antideuteron fluxes in cosmic rays.

Appendix A

Appendix A - Measurement results and EPOS predictions

A.1 NA61

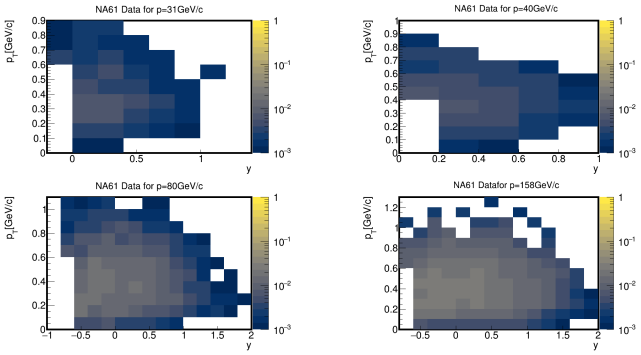

Figure A.1 Particle multiplicities normalized to the phase-space bin size $\frac{\mathrm{d}^2 n}{\mathrm{d}p_\mathrm{T}\mathrm{d}y}$ as a function of rapidity y and transverse momentum p_T as published by NA61

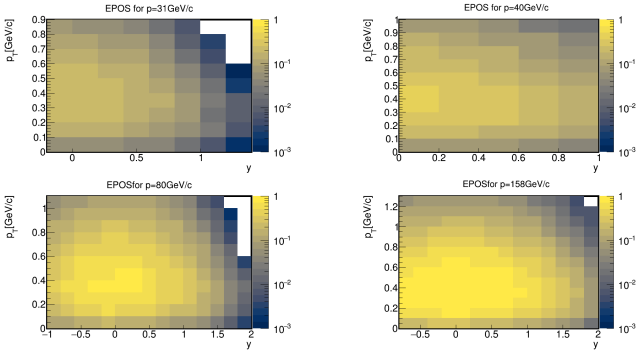

Figure A.2 EPOS predictions for particle multiplicities normalized to the phase-space bin size $\frac{\mathrm{d}^2 n}{\mathrm{d}p_\mathrm{T}\mathrm{d}y}$.

A.2 NA49

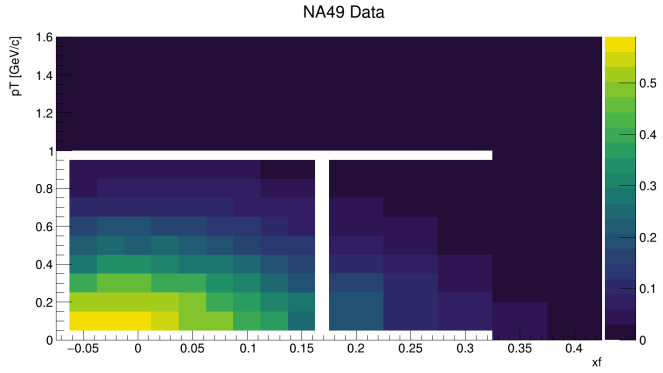

Figure A.3 The invariant cross section for inclusive antiproton production measured by NA49

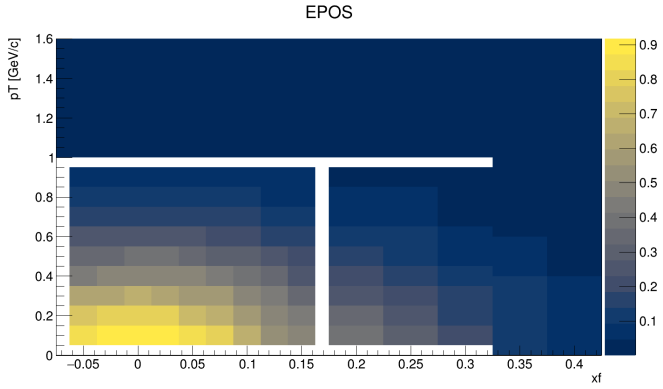

Figure A.4 Prediction of the invariant cross section for inclusive antiproton production by EPOS

A.3 LHCb p–He

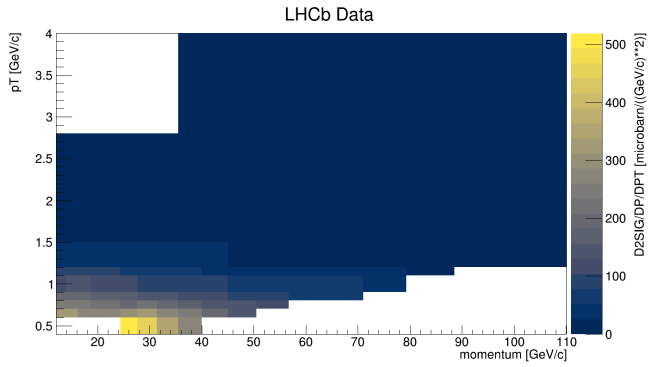

Figure A.5 Invariant inclusive antiproton production cross-section as measured by LHCb

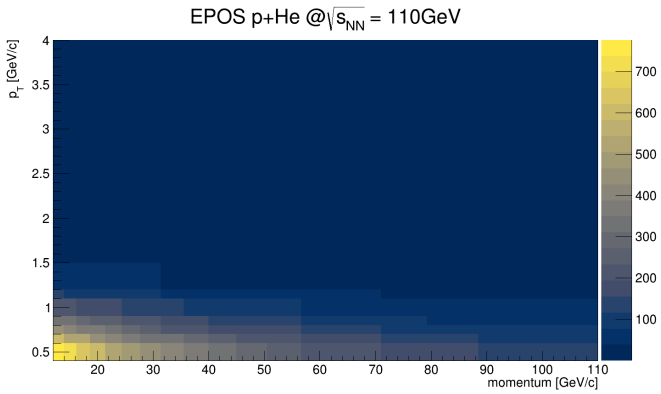

Figure A.6 Prediction for invariant inclusive antiproton production cross-section by EPOS

Appendix B

Appendix B - EPOS

B.1 Impact parameter in EPOS

The impact parameter can be obtained in two different ways. The easy way is by the *bim* parameter. This parameter gives back the impact parameter for each event, if in the EPOS configuration the *fillTree(C1)* option was chosen (See Fig. B.1 last line). If the *fillTree(C2)* option was used, then *bim* will give back the number of created pomerons. In order to then retrieve the impact parameter one needs to search in the output file. An example is shown in Fig. B.2. In this example EPOS created 7 Pomerons at an impact parameter of $b = 0.24$fm. In order to connect the impact parameter with its event one needs to look once again at the config file(Fig. B.1). The three lines above *fillTree(C2)* correspond to the three options discussed above. Each line contains the parameter *nfull* which defines the number of impact parameters created for each output file. Each impact parameter will then be used by *nfreeze* events in a row. So in this example the option for HYDRO+HACASwas chosen with 10 impact parameters for 10 events each creating a total of 100 events.

```
set laproj 1 set maproj 1 set latarg 2 set matarg 4  set ecms 220.2
set bminim 0 set bmaxim 2.4
set istmax 25  set phimin 0  set phimax 0
set ninicon 1 set iranphi 0 ftime on
set seedj 652094555
nodecays 110 20 2130 -2130 2230 -2230 1130 -1130 1330 -1330 2330 -2330 3331 -3331  end

! uncomment one of the following lines

!core full hydro x3ff   hacas off  set nfull 10    set nfreeze 10 set modsho 100   set centrality 0  set ijetfluid 1  !hydro
core full hydro x3ff   hacas full set nfull 10    set nfreeze 10 set modsho 100   set centrality 0  set ijetfluid 1  !hydro+casc
!core off hydro x3ffoff hacas off  set nfull 30000 set nfreeze 1  set modsho 1000 set centrality 0                    !no hydro no casc

fillTree(C2)
```

Figure B.1 An example of the EPOS config file

B.2 Concrete examples for particle groups of interest

•Primary antiprotons

Primary antiprotons (id=-1120) have no mother (ior=0) and depending on use case with particles from strong decays (no filering for fzus) and without (fzus!=-999)

```
################################################################################
ini  1:      1 its to get    1 Poms,  b =  1.58 ,  ptrevt =    3.6
dump cptl ...  done
utrescxx: p4 =   0.29802E-07  -0.14901E-06  -0.33027E+03   0.55046E+03
jintpo - ttaus fxcell fzcell nsegce:   0.10   4.00   1.00   4
delxce delsce vocell:  0.507692277       9.69833732E-02   2.49976031E-02
xcell,m1cell,zcell,m3cell:  3.30  13 10.18  21
 +++++Eall+++++(jintpo start)              3                      550.5
 +++++Eall+++++(jintpo start check highpt)                        550.5
calculate inicon table based on      1  ico-events ...
ico-event       1   bimevt:  1.58   seedf:     0.9574000000000000D+04
```

Figure B.2 An example of the EPOS output file, where b is the impact parameter and $poms$ the number of pomerons.

•Antiprotons from antilambda decays

For this a little more than just filtering for flags is required. First one needs to make a list of all indices of $\bar{\Lambda}$ in the event (id=-2230). Then one needs to filter for the $\bar{b}$ from decays (id=-1120, ior>0) and check if their value of ior is in the list of $\bar{\Lambda}$ indices. This can be done at runtime, since the particles which come from decays will always be below their mothers in the output. This can be similarly done for $\bar{b}$ from $\bar{\Sigma}^{-}$ decays.

Bibliography

[1] F. Zwicky, "Die Rotverschiebung von extragalaktischen Nebeln," *Helvetica Physica Acta*, vol. 6, pp. 110–127, Jan. 1933. *cited in 1 (p. 1)*

[2] G. Bertone and D. Hooper, "History of dark matter," *Reviews of Modern Physics*, vol. 90, Oct 2018. *cited in 1 (p. 1)*

[3] D. H. Rogstad and G. S. Shostak, "Gross Properties of Five Scd Galaxies as Determined from 21-CENTIMETER Observations," *apj*, vol. 176, p. 315, Sept. 1972. *cited in 1 (p. 1)*

[4] A. Bosma, *The distribution and kinematics of neutral hydrogen in spiral galaxies of various morphological types*. PhD thesis, -, Jan. 1978. *cited in 1 (p. 1)*

[5] V. C. Rubin *et al.*, "Extended rotation curves of high-luminosity spiral galaxies. IV. Systematic dynamical properties, Sa -> Sc.," *apjl*, vol. 225, pp. L107–L111, Nov. 1978. *cited in 1 (p. 1)*

[6] *Particle Dark Matter: Observations, Models and Searches*. Cambridge University Press, 2010. *cited in 1 (p. 1), 1 (p. 2)*

[7] P. D. Group *et al.*, "Review of Particle Physics," *Progress of Theoretical and Experimental Physics*, vol. 2020, 08 2020. 083C01. *cited in 1 (p. 1), 1 (p. 2)*

[8] H. Baer, K.-Y. Choi, J. E. Kim, and L. Roszkowski, "Dark matter production in the early universe: Beyond the thermal wimp paradigm," *Physics Reports*, vol. 555, p. 1–60, Feb 2015. *cited in 1.1 (p. 2)*

[9] A. Ibarra and S. Wild, "Prospects of antideuteron detection from dark matter annihilations or decays at ams-02 and gaps," *Journal of Cosmology and Astroparticle Physics*, vol. 2013, p. 021–021, Feb 2013. *cited in 1 (p. 3)*

[10] A. Cuoco *et al.*, "Novel dark matter constraints from antiprotons in light of ams-02," *Phys. Rev. Lett.*, vol. 118, p. 191102, May 2017. *cited in 1.3 (p. 4)*

[11] F. Donato, N. Fornengo, D. Maurin, P. Salati, and R. Taillet, "Antiprotons in cosmic rays from neutralino annihilation," *Phys. Rev. D*, vol. 69, p. 063501, Mar 2004. *cited in 1.3 (p. 4), 2.5 (p. 16), 2.3 (p. 16)*

[12] H. Fuke *et al.*, "Search for cosmic-ray antideuterons," *Physical Review Letters*, vol. 95, Aug 2005. *cited in 1.3 (p. 4)*

[13] T. Aramaki *et al.*, "Review of the theoretical and experimental status of dark matter identification with cosmic-ray antideuterons," *Physics Reports*, vol. 618, p. 1–37, Mar 2016. *cited in 1.3 (p. 4), 2.5 (p. 16)*

[14] T. Aramaki *et al.*, "Antideuteron sensitivity for the gaps experiment," *Astroparticle Physics*, vol. 74, p. 6–13, Feb 2016. *cited in 1.3 (p. 4), 2.5 (p. 16)*

[15] Korsmeier *et al.*, "Prospects to verify a possible dark matter hint in cosmic antiprotons with antideuterons and antihelium," *Physical Review D*, vol. 97, May 2018. *cited in 1.3 (p. 4), 1.4 (p. 5), 2.3 (p. 16)*

[16] L. Barioglio, *Study of the production of (anti-)deuterons in pp collisions at the LHC with the ALICE experiment.* PhD thesis, Feb 2020. Presented 08 May 2020. *cited in 2.1 (p. 7), 2.1 (p. 8), 2.2.1 (p. 8), 2.2.1 (p. 9)*

[17] U. W. Heinz, "Concepts of Heavy-Ion Physics," *arXiv*, Jul 2004. *cited in 2.1 (p. 7)*

[18] S. Mrówczyński, "Production of light nuclei in the thermal and coalescence models," *Acta Physica Polonica B*, vol. 48, no. 4, p. 707, 2017. *cited in 2.2.1 (p. 8)*

[19] S. Acharya, D. Adamová, J. Adolfsson, M. M. Aggarwal, G. A. Rinella, M. Agnello, N. Agrawal, Z. Ahammed, S. U. Ahn, S. Aiola, *et al.*, "Production of ^{4}he and $^4\bar{H}e$ in pb–pb collisions at $\sqrt{s_{\mathrm{NN}}}$= 2.76 tev at the lhc," *Nuclear Physics A*, vol. 971, pp. 1–20, 2018. *cited in 2.2 (p. 9)*

[20] S. T. Butler and C. A. Pearson, "Deuterons from high-energy proton bombardment of matter," *Phys. Rev.*, vol. 129, pp. 836–842, Jan 1963. *cited in 2.2.2 (p. 9)*

[21] N. Fornengo *et al.*, "Dark matter searches with cosmic antideuterons: status and perspectives," *J. Cosmol. Astropart. Phys.*, vol. 2013, p. 031, Sep 2013. *cited in 2.2.2 (p. 9)*

[22] D. M. Gomez Coral, *Deuteron and antideuteron production in galactic cosmic-rays. Producción de deuterio y antideuterio en rayos cósmicos galácticos.* PhD thesis, Mar 2019. Presented 26 Apr 2019. *cited in 2.2.2 (p. 9)*

[23] R. Scheibl and U. Heinz, "Coalescence and flow in ultrarelativistic heavy ion collisions," *Phys. Rev. C*, vol. 59, pp. 1585–1602, Mar 1999. *cited in 2.2.2 (p. 10), 2.2.2 (p. 11)*

[24] E. Wigner, "On the quantum correction for thermodynamic equilibrium," *Phys. Rev.*, vol. 40, pp. 749–759, Jun 1932. *cited in 2.2.2 (p. 10)*

[25] A. Ibarra and S. Wild, "Determination of the cosmic antideuteron flux in a monte carlo approach," *Phys. Rev. D*, vol. 88, p. 023014, Jul 2013. *cited in 2.2.2 (p. 11)*

[26] M. Kachelrieß, S. Ostapchenko, and J. Tjemsland, "Alternative coalescence model for deuteron, tritium, helium-3 and their antinuclei," *The European Physical Journal A*, vol. 56, Jan 2020. *cited in 2.2.2 (p. 11)*

[27] T. Aramaki *et al.*, "Review of the theoretical and experimental status of dark matter identification with cosmic-ray antideuterons," *Phys. Rep.*, vol. 618, pp. 1–37, Mar 2016. *cited in 2.3 (p. 13), 2.3 (p. 16)*

[28] T. Sjöstrand *et al.*, "An Introduction to PYTHIA 8.2," *arXiv*, Oct 2014. *cited in 2.2.3 (p. 13)*

[29] M. Bahr *et al.*, "Herwig++ Physics and Manual," *arXiv*, Mar 2008. *cited in 2.2.3 (p. 13)*

[30] S. Acharya *et al.*, "Search for a common baryon source in high-multiplicity pp collisions at the lhc," *Physics Letters B*, vol. 811, p. 135849, Dec 2020. *cited in 2.2.3 (p. 14), 2.2.3 (p. 14), 5.3 (p. 48), 5.6 (p. 49)*

[31] L. Barioglio, "Production of (anti)(hyper)nuclei at the lhc," 2021. LHCP2021. *cited in 2.2.4 (p. 15), 2.4 (p. 15)*

[32] M. M. Kachelrieß, S. Ostapchenko, and J. Tjemsland, "Revisiting cosmic ray antinuclei fluxes with a new coalescence model," *Journal of Cosmology and Astroparticle Physics*, vol. 2020, p. 048–048, Aug 2020. *cited in 2.3 (p. 16), 2.5 (p. 16)*

[33] M. di Mauro *et al.*, "New evaluation of the antiproton production cross section for cosmic ray studies," *Phys. Rev. D*, vol. 90, p. 085017, Oct 2014. *cited in 2.3 (p. 16), 4.5 (p. 37)*

[34] R. Kappl *et al.*, "Ams-02 antiprotons reloaded," *Journal of Cosmology and Astroparticle Physics*, vol. 2015, p. 034–034, Oct 2015. *cited in 2.5 (p. 16), 2.3 (p. 16)*

[35] K. Werner, "The hadronic interaction model EPOS," *Nucl. Phys. B Proc. Suppl.*, vol. 175-176, pp. 81–87, Jan 2008. *cited in 3 (p. 17)*

[36] R. D. Woods and D. S. Saxon, "Diffuse surface optical model for nucleon-nuclei scattering," *Phys. Rev.*, vol. 95, pp. 577–578, Jul 1954. *cited in 3.1 (p. 17)*

[37] E. Levin, "Everything about reggeons.Part I:Reggeons in "soft" interaction," *arXiv*, Oct 1997. *cited in 3.1 (p. 17)*

[38] T. Regge, "Introduction to complex orbital momenta," *Nuovo Cim.*, vol. 14, pp. 951–976, Dec 1959. *cited in 3.1 (p. 17)*

[39] S. Porteboeuf, T. Pierog, and K. Werner, "Producing hard processes regarding the complete event: The epos event generator," 2010. *cited in 3.1 (p. 18)*

[40] M. Bleicher *et al.*, "Relativistic hadron-hadron collisions in the ultra-relativistic quantum molecular dynamics model," *Journal of Physics G: Nuclear and Particle Physics*, vol. 25, p. 1859–1896, Sep 1999. *cited in 3.1 (p. 18), 3.2 (p. 19)*

[41] Jan 2018. [Online; accessed 28. Jun. 2021]. *cited in ?? (p. 19)*

[42] G. Sophys, *Formation of Quark-Gluon-Plasma: Understanding the energy and system size dependence*. PhD thesis, UNIVERSITE DE NANTES, 2018. *cited in 3.2 (p. 19), 3.2 (p. 21)*

[43] Dec 2019. [Online; accessed 30. Jun. 2021]. *cited in 3.2 (p. 21)*

[44] A. Aduszkiewicz *et al.*, "Measurements of , K, p and spectra in proton-proton interactions at 20, 31, 40, 80 and 158 with the NA61/SHINE spectrometer at the CERN SPS," *Eur. Phys. J. C*, vol. 77, pp. 671–41, Oct 2017. *cited in ?? (p. 23), 4 (p. 24), 4.1.1 (p. 24), 4.1.1 (p. 25)*

[45] The NA49 Collaboration, T. Anticic, *et al.*, "Inclusive production of protons, anti-protons and neutrons in p+p collisions at 158 GeV/c beam momentum," *Eur. Phys. J. C*, vol. 65, pp. 9–63, Nov 2009. *cited in* **??** *(p. 23), 4 (p. 24), 4.1.2 (p. 26), 4.1.2 (p. 26)*

[46] The NA49 Collaboration, B. Baatar, *et al.*, "Inclusive production of protons, anti-protons, neutrons, deuterons and tritons in p+C collisions at 158 GeV/c beam momentum," *arXiv*, Jul 2012. *cited in* **??** *(p. 23), 4 (p. 24), 4.2.1 (p. 31)*

[47] LHCb collaboration, R. Aaij, *et al.*, "Measurement of antiproton production in pHe collisions at $\sqrt{s_{NN}} = 110$ GeV," *arXiv*, Aug 2018. *cited in* **??** *(p. 23), 4 (p. 24), 4.2.2 (p. 32)*

[48] BRAHMS Collaboration, I. Arsene, *et al.*, "Production of Mesons and Baryons at High Rapidity and High p_T in Proton-Proton Collisions at $\sqrt{s} = 200$ GeV," *Phys. Rev. Lett.*, vol. 98, p. 252001, Jun 2007. *cited in* **??** *(p. 23), 4 (p. 24), 4.1.3 (p. 29), 4.7 (p. 29)*

[49] STAR Collaboration, J. Adams, *et al.*, "Identified particle distributions in pp and Au+Au collisions at sqrt{s_NN}=200 GeV," *arXiv*, Oct 2003. *cited in* **??** *(p. 23),* **??** *(p. 23), 4 (p. 24), 4.1.4 (p. 29), 4.2.3 (p. 33)*

[50] M.-Y. Cui *et al.*, "Revisit of cosmic ray antiprotons from dark matter annihilation with updated constraints on the background model from ams-02 and collider data," *Journal of Cosmology and Astroparticle Physics*, vol. 2018, p. 024–024, Jun 2018. *cited in 4.1 (p. 24)*

[51] L. Šerkšnytė, "Simulation of cosmic-ray antimatter fluxes," Master's thesis, Oct 2019. *cited in 4 (p. 24), 4.2 (p. 30), 6 (p. 51)*

[52] AMS Collaboration *et al.*, "Antiproton Flux, Antiproton-to-Proton Flux Ratio, and Properties of Elementary Particle Fluxes in Primary Cosmic Rays Measured with the Alpha Magnetic Spectrometer on the International Space Station," *Phys. Rev. Lett.*, vol. 117, p. 091103, Aug 2016. *cited in 4 (p. 24), 4.2 (p. 25)*

[53] M. Korsmeier, *Unveiling dark matter with cosmic messengers*. PhD thesis, Oct 2020. *cited in 4.1.3 (p. 29)*

[54] M. W. Winkler, "Cosmic Ray Antiprotons at High Energies," *arXiv*, Jan 2017. *cited in 4.1.3 (p. 29), 4.1.4 (p. 30), 4.5 (p. 37), 6 (p. 51)*

[55] STAR Collaboration, "Beam energy dependence of (anti-)deuteron production in Au+Au collisions at RHIC," *arXiv*, Mar 2019. *cited in 4.2.3 (p. 33),* **??** *(p. 43), 5.2 (p. 44), 5.2 (p. 46)*

[56] STAR Collaboration, B. I. Abelev, *et al.*, "Systematic measurements of identified particle spectra in pp, $d+$Au, and Au$+$Au collisions at the STAR detector," *Phys. Rev. C*, vol. 79, p. 034909, Mar 2009. *cited in 4.2.3 (p. 33), 4.12 (p. 34)*

[57] The NA49 Collaboration, "Inclusive production of charged pions in p+p collisions at 158 GeV/c beam momentum," *Eur. Phys. J. C*, vol. 45, pp. 343–381, Feb 2006. *cited in 4.3 (p. 35)*

[58] C. Chen *et al.*, *Scientific Computing with Radial Basis Functions*. Sep 2007. *cited in 4.5 (p. 38)*

[59] PHENIX Collaboration *et al.*, "Identified charged hadron production in $p+p$ collisions at $\sqrt{s}=200$ and 62.4 GeV," *Phys. Rev. C*, vol. 83, p. 064903, Jun 2011. *cited in 4.7 (p. 41)*

[60] D. Dekkers *et al.*, "Experimental Study of Particle Production at Small Angles in Nucleon-Nucleon Collisions at 19 and 23 GeV/c," *Phys. Rev.*, vol. 137, pp. B962–B978, Feb 1965. *cited in 4.7 (p. 41)*

[61] P. Capiluppi *et al.*, "Charged particle production in proton-proton inclusive reactions at very high energies," *Nucl. Phys. B*, vol. 79, pp. 189–258, Sep 1974. *cited in 4.7 (p. 41)*

[62] K. Guettler *et al.*, "Inclusive production of low-momentum charged pions, kaons, and protons at x = 0 at the CERN intersecting storage rings," *Nucl. Phys. B*, vol. 116, pp. 77–98, Dec 1976. *cited in 4.7 (p. 41)*

[63] J. R. Johnson *et al.*, "Inclusive Production of $\pi^{\pm}$, $K^{\pm}$, p, $\overline{p}$ in High-Energy $p-p$ Collisions," *Phys. Rev. Lett.*, vol. 39, pp. 1173–1176, Nov 1977. *cited in 4.7 (p. 41)*

[64] D. Antreasyan *et al.*, "Production of hadrons at large transverse momentum in 200-, 300-, and 400-GeV $p-p$ and p-nucleus collisions," *Phys. Rev. D*, vol. 19, pp. 764–778, Feb 1979. *cited in 4.7 (p. 41)*

[65] S. Acharya *et al.*, "Production of deuterons, tritons, he3 nuclei, and their antinuclei in pp collisions at s=0.9 , 2.76, and 7 tev," *Physical Review C*, vol. 97, Feb 2018. *cited in ?? (p. 43), 5.3 (p. 47), 5.8 (p. 50)*

[66] S. Acharya *et al.*, "Multiplicity dependence of light (anti-)nuclei production in p–pb collisions at snn=5.02 tev," *Physics Letters B*, vol. 800, p. 135043, Jan 2020. *cited in ?? (p. 43)*

[67] T. Anticic *et al.*, "Antideuteron and deuteron production in midcentral pb+pb collisions at 158a gev," *Phys. Rev. C*, vol. 85, p. 044913, Apr 2012. *cited in ?? (p. 43)*

[68] I. Arsene, I. G. Bearden, D. Beavis, S. Bekele, C. Besliu, B. Budick, H. Bøggild, C. Chasman, C. H. Christensen, P. Christiansen, and et al., "Rapidity dependence of deuteron production in centralau+aucollisions atsnn=200gev," *Physical Review C*, vol. 83, Apr 2011. *cited in ?? (p. 43)*

[69] S. S. Adler, S. Afanasiev, C. Aidala, N. N. Ajitanand, Y. Akiba, J. Alexander, R. Amirikas, L. Aphecetche, S. H. Aronson, R. Averbeck, and et al., "Deuteron and antideuteron production in au+au collisions atsnn=200gev," *Physical Review Letters*, vol. 94, Apr 2005. *cited in ?? (p. 43)*

[70] C. Adler *et al.*, "$\overline{d}$ and $^3\overline{\mathrm{he}}$ production in $\sqrt{s_{\mathrm{NN}}}=130GeVAu+Au$ collisions," *Phys. Rev. Lett.*, vol. 87, p. 262301, Dec 2001. *cited in ?? (p. 43)*

[71] I. G. Bearden *et al.*, "Antideuteron production in 158AGeV/c Pb + Pb collisions," *Phys. Rev. Lett.*, vol. 85, pp. 2681–2684, Sep 2000. *cited in ?? (p. 43)*

[72] T. A. Armstrong *et al.*, "Antideuteron yield at the ags and coalescence implications," *Phys. Rev. Lett.*, vol. 85, pp. 2685–2688, Sep 2000. *cited in ?? (p. 43)*

[73] Y. M. Antipov *et al.*, "Production of low momentum negative particles by 70 gev protons," *Phys. Lett. B*, vol. 34, pp. 164–166, 1971. *cited in 5.1 (p. 43)*

[74] P. Stankus *et al.*, "anti-p and anti-d production in relativistic heavy ion collisions: Results of BNL-E858," *Nucl. Phys. A*, vol. 544, pp. 603C–608C, 1992. *cited in 5.1 (p. 43)*

[75] B. Alper *et al.*, "Large angle production of stable particles heavier than the proton and a search for quarks at the cern intersecting storage rings," *Physics Letters B*, vol. 46, no. 2, pp. 265–268, 1973. *cited in 5.1 (p. 43)*

[76] J. Adams *et al.*, "Pion interferometry in Au+Au collisions at S(NN)**(1/2) = 200-GeV," *Phys. Rev. C*, vol. 71, p. 044906, 2005. *cited in 5.1 (p. 45)*

[77] "GALPROP." *cited in 6 (p. 51)*